applied sciences

MDPI

*Review*

# Metal-Organic Frameworks Characterization via Inverse Pulse Gas Chromatography

**Kareem Yusuf [1,*], Osama Shekhah [2,*], Zeid ALOthman [1] and Mohamed Eddaoudi [2]**

[1] Department of Chemistry, College of Science, King Saud University, P.O. Box 2455, Riyadh 11451, Saudi Arabia; zaothman@ksu.edu.sa

[2] Advanced Membranes and Porous Materials Centre (AMPMC), Physical Sciences and Engineering Division, Functional Materials Design, Discovery and Development Research Group (FMD3), King Abdullah University of Science and Technology (KAUST), P.O. Box 6900, Jeddah 23955, Saudi Arabia; mohamed.eddaoudi@kaust.edu.sa

* Correspondence: kmahmoud@ksu.edu.sa (K.Y.); Osama.shekhah@kaust.edu.sa (O.S.); Tel.: +966-56-137-1903 (K.Y.); +966-54-470-0625 (O.S.)

**Abstract:** The desire to customize the properties of a material through complete control over both its chemical and architectural structure has created a constant and persistent need for efficient and convenient characterization techniques. Inverse gas chromatography (IGC) is considered a useful characterization method for probing the material's surface properties, like its enthalpies of adsorption, which are the key stimulus components for their adsorption performance. Here, we conclusively review the significance of a less common application of the IGC technique for the physicochemical characterization of metal-organic frameworks (MOFs), which are an innovative subclass of porous materials with matchless properties in terms of structure design and properties. This review focuses on the fundamental theory and instrumentation of IGC as well as its most significant applications in the field of MOF characterization to shed more light on this unique technique.

**Keywords:** inverse gas chromatography; IGC; metal-organic frameworks; dispersive surface properties; specific surface properties; physicochemical characterization

check for updates

**Citation:** Yusuf, K.; Shekhah, O.; ALOthman, Z.; Eddaoudi, M. Metal-Organic Frameworks Characterization via Inverse Pulse Gas Chromatography. *Appl. Sci.* **2021**, *11*, 10243. https://doi.org/10.3390/app112110243

Academic Editor: Carolina Belver

Received: 14 October 2021
Accepted: 28 October 2021
Published: 1 November 2021

**Publisher's Note:** MDPI stays neutral with regard to jurisdictional claims in published maps and institutional affiliations.

**Copyright:** © 2021 by the authors. Licensee MDPI, Basel, Switzerland. This article is an open access article distributed under the terms and conditions of the Creative Commons Attribution (CC BY) license (https://creativecommons.org/licenses/by/4.0/).

## 1. Introduction

To help identify the potential application of a microporous solid in separation or catalysis, theoretical or experimental determination of its basic adsorption properties and sorption behavior is a beneficial tool. Gathering information about the surface activity of these microporous materials provides a deeper understanding of their performance and continual development. Consequently, it is important to determine the surface properties that indicate the surface's ability to contribute to both dispersive and specific interactions.

The adsorption enthalpy and associated physicochemical parameters of a material may be derived directly from calorimetric measurements or indirectly by the adsorption constant temperature dependence obtained by volumetric, gravimetric, or chromatographic adsorption measurements [1–9]. Alkane adsorption molecular modeling via force fields for zeolites has been improved to such an extent over the last decade that great canonical Monte Carlo models can now be applied to forecast zeolites' adsorption behavior at high levels of pore filling [10–12].

Inverse gas chromatography (IGC) is recognized as a proper and fast tool for characterizing the surface properties of porous solids, with a minimal adsorbent amount needed for reliable calculations and shorter experimental times compared to other techniques used for thermodynamic characterization. One of the unique features of IGC is that no specific or complicated preparation procedure of samples is necessary. Relative to other surface energy analysis techniques, IGC requires minimal sample preparation [13]. One can easily and accurately use the IGC technique to characterize various crystalline, composite, amorphous, or even fibrous solids.

Without the need for any extrapolation, the enthalpies of adsorption measured with IGC and other methods show excellent consistency [14–16]. Since IGC has a superior efficiency at infinite dilution, it can differentiate between characteristic variations that other methods, such as conventional wettability measurements, do not identify [15]. For example, the probability of observing the differences associated with surface group orientations is one advantage of using IGC in researching acid–base specific properties [15].

Compared to analytical gas chromatography (GC), the mobile and stationary phases and roles are reversed in IGC. In IGC, the explored material represents the stationary phase. The injected known molecules within the mobile phase are considered probes used to investigate the physicochemical properties of the stationary phase.

The first attempt to introduce IGC was by Nobel Laureates Martin and Synge in 1941 [17]. In 1960, Kiselev gave the emerged IGC technique its name [18]. Furthermore, he was a key player in developing chromatography and the field of surface chemistry [19]. GC was identified by Smidsrod and Guillet as a versatile "indispensable analytical instrument" for applications other than defining mixture constituents [20]. In the 1970s, IGC became more familiar when it proved to be a promising method in investigating the surface and bulk properties of polymers and related materials [21]. Polymeric studies are still the most significant application of IGC judging by the large number of related publications [22].

In principle, IGC experiments can be conducted by either a pulse or frontal technique. For a pulse technique, a specific portion of the tested molecule is injected. With the help of a carrier gas, this pulse is transferred across the system through a column that is packed with the studied material. A chromatographic peak appears as a result of the adsorption and desorption processes within the column. On the other hand, in the frontal technique, the tested molecule is injected perpetually into the system, and consequently, a breakthrough curve will be the output chromatogram [21]. The advantage of the frontal technique is that, due to its continuous operation, equilibrium can be achieved, whereas the pulse technique relies on the assumption of rapid equilibrium between the probe and the solid surface.

In the case of the continuous flow method, which is a classical form of frontal technique [23], the column can be detached from the gas flow if the concentration is changed and afterwards attached again when the flow is balanced. Then, a positive peak will appear for a higher concentration and adsorption process, while a negative peak will indicate a lower concentration and desorption process. The peak area is directly proportional to the amount of adsorption or desorption. This technique is utilized in many instruments conceived for the dynamic estimation of Brunauer–Emmett–Teller (BET) surface area [15]. However, this approach cannot be considered an IGC technique since retention time is not a parameter in the experimental calculations [15]. In comparison, classical frontal experiments evaluate the nature of retention and, therefore, are considered an IGC technique.

A significant proportion of publications utilized pulse instead of frontal approaches because they are quicker, more convenient, and provide higher accuracy, especially if there are poor interactions between the tested material and probe. The frontal approach is a suitable alternative if a slow equilibrium is the topic of examination.

Some research groups tend to prefer the term "pulse gas chromatography" over the term "inverse gas chromatography," while others used the full expression "inverse pulse gas chromatography." We have noticed that these different terminologies were sometimes misleading, indicated by few cross citations. Furthermore, subsequent studies claim that "*there have been almost no studies using the IGC with MOFs*" [24].

After the IGC technique was recognized as a sensitive and simple tool for investigating physicochemical properties, it was applied for different types of materials, including non-volatile and solid materials with numerous morphologies. For instance, it was applied to evaluate the impact of grinding on the surface and bulk features of drug molecules [25], which is important for medicinal industry improvements. IGC has also been used to deconvolve the chemical and structural properties of carbon nanotube surfaces [26]. Additionally, IGC was used to characterize polymers, minerals, modified silicas, surfactants, and zeolites [22,27]. However, in the case of metal–organic frameworks (MOFs), which

are considered a recently introduced porous material, few studies have used IGC for the characterization of their different properties.

Metal-organic frameworks (MOFs) are a subclass of porous crystalline materials constructed by linking metallic nodes like single-ion or clusters with organic linkers. They have been developed in the last twenty years as potential candidates for solving many of the challenges associated with different applications, such as gas storage, separation, catalysis, and sensing [28–30], by means of the anticipated on-demand control of their pore-system (i.e., pore-aperture, shape, size, and functionality). MOFs are considered organic-inorganic hybrid porous materials and have supreme chemical, structural, and topological adaptability [31,32]. Their pore system is tunable via different design and engineering strategies [33]. MOFs can be efficiently designed with the proper properties in terms of pore aperture size, controlled by the organic linkers linked through metallic-nodes and/or shape (channels or cages), to achieve the targeted application. Successful exercising of reticular chemistry ensures the suitable inorganic and organic building blocks, encompassing defined geometrical information that ciphers a designated net, are constructed into a hybrid material framework with the desired topology.

MOFs with a wide range of porosities and chemical functionalities have been synthesized and explored in many applications such as separation and catalysis [30,34]. Separation, for example, can be driven by the difference in affinities and interactions between the MOF framework and the targeted probe molecules, where the structure and chemical functionality of the MOF pores can be varied, for example, via the organic linker length, functionalization, or integration of coordinatively unsaturated metal sites [35–37]. MOFs have demonstrated outstanding performances as separating agents either as adsorbents or membranes as a result of their well-defined chemical and structural properties in terms of pore size, functionality, and rigidity/flexibility, which correlate with the targeted adsorbates' intrinsic properties like functionality, size, shape, etc.

Porous materials like MOFs that possess essential features for the selective separation of targeted analytes over others represent a potential alternative to energy-intensive techniques like distillation. An adsorption-based process can afford separation via thermodynamics, where the MOF acts as an adsorbent and shows a comparatively high affinity for a particular molecule due to the enhanced interactions between the adsorbates and the MOF material.

Due to their unique surface properties and separation abilities, much research is focused on using MOFs in applications like sensing, catalysis, or as separating agents for carbon-capture, hydrocarbons separation, xenon/krypton, and many other essential separations.

This study sums up past work concerning the utilization of IGC as a characterization tool to investigate the physicochemical features of MOFs and highlights IGC as a useful, revolutionary, and almost undiscovered technique for investigating and predicting the adsorption properties of MOFs.

## 2. Fundamentals of Inverse Gas Chromatography (IGC)

### *2.1. Instrumentation and Methods*

In analytical GC, the tested sample mixture, whether gas or liquid, is injected into a well-defined analytical column to separate the composition of that mixture for subsequent qualitative and quantitative analysis. The mixture is separated through different interactions of varying strengths between the analytes and the stationary phase. In IGC, a single known probe is usually injected into a packed column to study its retention behavior and correlation with the physicochemical properties of the packing material. Various probes with different well-known properties are used.

The composition of the IGC instrument is similar to that of the analytical GC technique (Figure 1). An IGC packed column may be glass, fused silica, copper, stainless steel, or Teflon. Wall-coated open-tubular long columns have also been used in several types of research. An inert carrier with a steady flow conducts the probe through the column at a

constant rate. In IGC, the main collected parameter is the retention time, which has been effectively used to evaluate the solid surface's dispersive properties and potential specific interactions [15,16,22].

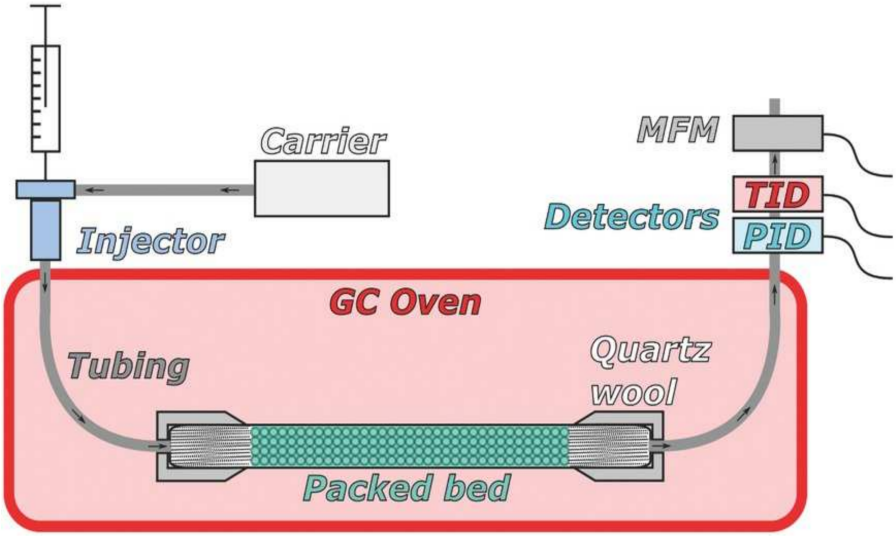



**Figure 1.** Schematic depiction of the IGC setup. Pressure sensors (before and after packed bed) and electronic pressure controller (before injector) omitted for clarity. MFM: mass flow meter. Reprinted with permission from [38] Copyright (2018) Elsevier.

IGC experiments can be carried out under two different conditions: infinite dilution and finite concentration. Infinite dilution has been identified as appropriate for the heat of sorption and surface energy examination of particles [39]. Infinite dilution at low surface coverage indicates a minimal amount of the tested probe molecule is injected. A low concentration of the adsorbate molecules indicates that the interactions occur with the higher energy sites available at the surface of tested materials. Furthermore, probe-to-probe interactions are considered negligible due to the limited amount of the probe. Therefore, Henry's Law is applied [40], resulting in a linear isotherm of adsorption and a typical chromatographic peak [15,22]. Infinite dilution is the dominant condition in the IGC technique.

At finite concentration, a large amount of test probe is injected into the system; hence, interaction with all surface sites is expected [41]. This technique can be used to determine solids' heterogeneity of surface energy [42], or to study the role of both mesopores and micropores in adsorption and thermal desorption methods [43]. However, finite concentration IGC is out of the scope of this review.

### *2.2. Theory*

The surfaces of solids are normally characterized by their dispersive and specific properties. By measuring the dispersive components of the surface free energy, the dispersive nature is obtained. Specific properties are defined by the factors that calculate the surface propensity to exhibit Lewis acidic or basic features, thus indicating an electron acceptor or donor nature. The total solid surface energy is represented via the summation of both the dispersive and the specific properties.

#### 2.2.1. Dispersive Properties of the Surface

The retention volume ($V_N$) occupied by a carrier gas from the injection valve to the maximum of the chromatographic peak through the column is estimated using the following equation [44]:

$$V_N = (t_R - t_M)\, F_a \frac{T}{Ta} j \quad (1)$$

Here, $t_R$ represents the retention time and $t_M$ is the dead time, which is usually experimentally calculated by using an unretained methane gas probe. $F_a$ represents the volumetric flow rate, $T$ represents the column temperature, $T_a$ represents the ambient temperature, and $j$ represents the James-Martin gas compressibility correction factor, which can be calculated from Equation (2) [45]:

$$J = \frac{3(P^2 - 1)}{2(P^3 - 1)} \tag{2}$$

where $P$ represents $P_i/P_o$, with column pressure ($P_i$) and outlet pressure ($P_o$).

A specific retention volume ($V_g$) represents a definite value of the material (as a particular guest molecule-material) affected by several factors, including particle size, packing geometry, and temperature, among others. This is considered equivalent to the point of inflection in breakthrough experiments as an example of frontal techniques [22,46]. The following relationship (3) is used to calculate $V_g$:

$$V_g = \left[\frac{273.15\ (t_R - t_m)Fa\ j}{w\ T}\right]\left[\frac{(P_o - P_w)}{P_w}\right] = 3/2\left[\frac{273.15\ (t_R - t_m)Fa\ j}{w\ T}\right] \tag{3}$$

where $w$ represents the weight of the stationary phase, and $P_w$ represents the vapor pressure of water at the used $T$.

Conventionally, IGC basic equations are derived from $V_g$; however, the retention volume ($V_N$) is very often utilized as well. Additionally, $V_g$ could be estimated from the net $V_N$ through the following equation [47]:

$$V_g = \frac{V_N\ 273.15}{w\ T} \tag{4}$$

Henry constants ($K'$) represent the slope of isotherm in the linear region. They reflect the proportion of carrier inert gas that is needed to elute the corresponding analytes' maximum concentration within the porous material. Henry constants are usually determined using the retention volume $V_N$ and considering ideal analyte behavior [21,48]:

$$K' = \frac{V_N}{R\ T} \tag{5}$$

where $T$ represents the experimental temperature of the column, and the ideal gas constant is denoted by $R$.

The ability of the investigated material to discriminate branched alkanes from linear ones is a result of the dissimilarities in the tested probes' physicochemical properties or the material's selective shape properties. To determine the actual reason for the separation, the Henry constants logarithm could be compared to the vapor pressure logarithm plot. For linear alkanes, the relationship is linear; but after the branched alkanes are positioned in that line, the material cannot separate those probes based on their shape and vice versa [49].

The dispersive component of the surface energy ($\gamma_S^D$) reflects the capability of a solid surface to demonstrate Van der Waals forces or London interactions, and the surface heterogeneity of the probed material. It is a typical factor that estimates the energy of the surfaces of solids and is deemed the equivalent of surface tension in liquids [50]. Two major techniques are employed in order to determine the dispersive interactions between the probes and the tested solid phase: Dorris-Gray [51] and Schultz et al. methods [52]. Dorris-Gray proposed a relationship to estimate $\gamma_S^D$, relying on the Fowkes's approach [50] regarding the used stationary phase and adhesion of methylene group, as shown in Equation (6) [51]:

$$\gamma_S^D = \frac{1}{4\gamma_{CH2}}\left(\frac{RT\frac{V_{N,n+1}}{V_{N,n}}}{N\ a_{CH2}}\right)^2 \tag{6}$$

where $N$ represents Avogadro's number, the methylene group cross-sectional area is $a_{CH2}$ (≈6 Å$^2$), $V_{N,n+1}$ represent the net retention volumes for n-alkanes with carbon number $n + 1$ and $V_{N,n}$ for carbon atoms with only $n$, and $\gamma_{CH2}$ represents the surface dispersive free energy of only $CH_2$ groups (as, for example, in linear polyethylene), in a solid material calculated at a given $T$ (°C) using the following equation [52]:

$$\gamma_{CH2} = 35.6 - 0.058\, t \tag{7}$$

The Fowkes approach was also the base of the Schultz et al. method, in which the effect of adhesion represents the dispersive free energy between the stationary phase and the probe. Hence, Schultz et al. introduced a relationship between the surface dispersive free energy and $V_N$ as follows:

$$RT\ln V_N = 2Na\sqrt{\gamma_l^d \cdot \gamma_s^d} + K \tag{8}$$

where $a$ represents a cross-sectional area and $\gamma_l^d$ is the solute probe dispersive free energy. For n-alkanes, a linear relationship is obtained when $RT\ln V_N$ is plotted against $a\sqrt{\gamma_l^d}$. The dispersive free energy for the solute probe can be evaluated from the slope.

The enthalpy change of adsorption ($\Delta H_{ads}$) can be easily obtained by plotting the logarithm of the retention volume, the logarithm-specific retention volume, or Henry's constants gained from isothermal GC measurements versus the inverse temperature. The adsorption enthalpy change $\Delta H_{ads}$ (the differential heat of adsorption) represents the interaction strength between the adsorbed molecule and the adsorbent atoms at zero surface coverage:

$$\Delta H_{ads} = -R\ \frac{d\ln\ V_N}{d\ (1/T)} = -R\ \frac{d\ln\ V_g}{d\ (1/T)} \tag{9}$$

The standard free energy change of adsorption ($\Delta G_{ads}$) is determined from the $V_N$ or $V_g$ of the vapor probe using Equation (10) [44]:

$$\Delta G_{ads} = -RT\ln\left(\frac{V_N\ P^o}{m\ S\ \pi 0}\right) = \Delta G_{ads} = -RT\ln\left(\frac{V_g\ P^o}{S\ \pi 0}\right) \tag{10}$$

where $m$ represents the adsorbent material mass in the column, $\pi_0$ represents the reference two-dimensional surface pressure, $S$ represents the specific surface area of the adsorbent, $P^\circ$ represents the vapor pressure of the adsorbate in the gaseous state, which can be estimated using Antoine's equation:

$$\mathrm{Log}(P^\circ) = A - \left(\frac{B}{t + C}\right) \tag{11}$$

where $A$, $B$, and $C$ are the Antoine coefficients from the handbooks and $t$ is the temperature in Celsius.

The standard entropy change of adsorption ($\Delta S_{ads}$) is calculated at zero Henry surface coverage using the following equation:

$$\Delta S_{ads} = \frac{\Delta H_{ads} - \Delta G_{ads}}{T} \tag{12}$$

#### 2.2.2. Specific Properties of the Surface

Specific as well as dispersive interactions occur simultaneously for polar probes in the absence of metallic, magnetic, electrostatic, or acid–base surface interactions, which reflect most specific interactions [16]. Polar probes' free energy of adsorption has two types of interactions: dispersive interactions, which are symbolized by $\Delta G_{ads}^D$ and correspond to

London forces, and specific interactions, which are symbolized by $\Delta G_{ads}^{SP}$ and are attributed principally to Lewis acid–base contributions:

$$\Delta G_{ads} = \Delta G_{ads}^{D} + \Delta G_{ads}^{SP} \quad (13)$$

The free adsorption energy-specific component ($\Delta G_{ads}^{SP}$) is estimated as the difference between the polar compound free energy of adsorption ($\Delta G_{polar}$) and the free adsorption energy of hypothetical alkane ($\Delta G_{ref}$) (Equation (14)). The hypothetical alkane must have the same assigned property as a polar probe (e.g., vapor pressure in the Papirer method [53], boiling point in the Brookman and Sawyer method [54], or $a\sqrt{\gamma_l^d}$ value in Schultz and Lavielle method) (Figure 2):

$$\Delta G_{ads}^{SP} = \Delta G_{polar} - \Delta G_{ref} \quad (14)$$

where

$$\Delta G_{polar} = -RT \ln V_{N\,polar} + C \text{ and } \Delta G_{ref} = -RT \ln V_{N\,ref} + C$$

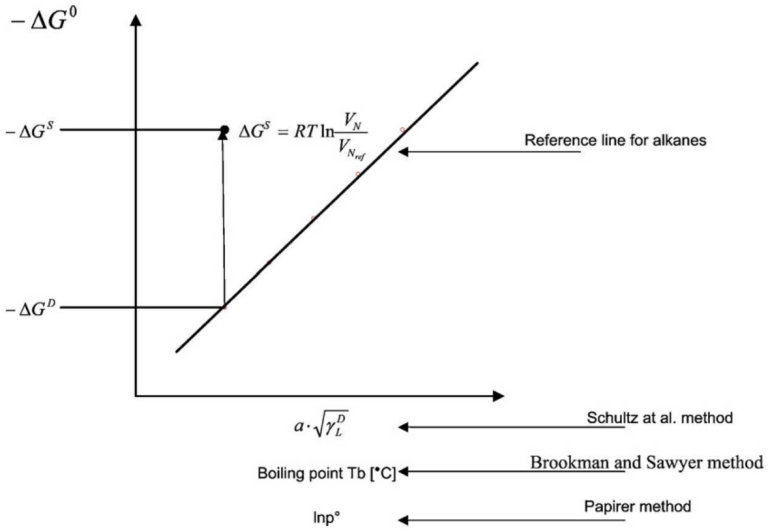



**Figure 2.** Different procedures for $\Delta G_{ads}^{SP}$ determination. Reprinted with permission from [16]. Copyright (2009) Elsevier.

The specific component of the adsorption enthalpy ($\Delta H_{ads}^{SP}$) is determined from the $\Delta G_{ads}^{SP}$ dependence on temperature, reflecting the Gibbs Helmholtz equation:

$$\Delta G_{ads}^{SP} = \Delta H_{ads}^{SP} - \Delta S_{ads}^{SP} \quad (15)$$

where the polar probe's specific component of adsorption entropy is represented by $\Delta S_{ads}^{SP}$. Hence, $\Delta H_{ads}^{SP}$ can be calculated from the slope of $\frac{\Delta G_{ads}^{SP}}{T}$ versus $\frac{1}{T}$.

The specific enthalpy of adsorption of a probe on the tested solid surface is correlated to the solid's acid–base properties. The acceptor constant ($K_A$) represents the acidity, and the donor constant ($K_D$) represents the basicity of the tested solid phase; both are determined using Equation (16):

$$\frac{\Delta H_{ads}^{SP}}{AN^*} = \frac{DN}{AN^*} K_A + K_D \quad (16)$$

where $AN^*$ is the modified acceptor number of Riddle and Fowkes [55], and $DN$ is Gutmann's donor number [56]. The value of $K_A$ is represented by the slope of the linear relation between $-\frac{\Delta H_{ads}^{SP}}{AN^*}$ *vs.* $\frac{DN}{AN^*}$, and the intercept corresponds to $K_D$.

## 3. Applications of IGC for the Characterization of MOFs

IGC is considered a very effective surface energy analysis tool for the characterization of various materials' surface properties. Here, we review recent applications of IGC in analyzing the surface properties of MOF materials. These applications include gases, hydrocarbons, and solvents, which reflect the wide-ranging advantages that can be achieved by applying the IGC technique (Table 1). The IGC evaluations reviewed here were are carried out using conventional GC at infinite dilution, which is usually equipped with a flame ionization detector (FID) or a thermal conductivity detector (TCD).

The studied MOFs were packed into either metallic or glass columns of 2–80 cm length, with 30 cm being the most commonly used length, and a standard internal diameter (ID) of 3.18 mm with actual utilization of the columns ranging from 0.53 to 5.3 mm ID (Table 1). Whether prepared or purchased, the adsorbent powder was either packed directly into the column or pressed under high pressure (~600 bar) into disks, then broken into fragments and sieved to the proper fraction for a higher homogeneity.

Packing of the tested material was achieved either through vacuum suction of the dry powder or by pushing the suspended powder into the empty tubing. In either case, good packing was usually accomplished using mechanical vibration or an ultrasonic water bath; thereafter, the column ends were plugged with glass wool to avoid the loss of adsorbent.

Silica wall-coated open tubular capillary columns have been used successfully for the IGC calculations for the coated material. Capillary columns coated with MOFs have been used in two forms: either a controlled approach using secondary building units (SBUs) for in situ preparation of the MOF material [24], or as a dynamic coating after preparation [73]. Estimating the physicochemical properties of MOFs incorporated into an organic monolithic capillary column as a composite is an unusual platform for IGC studies; however, it was successful [71].

Generally, high purity nitrogen or helium ($\geq$99.99%) is applied as the carrier gas with flow rates ranging from 20 to 60 mL $min^{-1}$; exceptions include 1 and 5.3 mL $min^{-1}$ flow rates, which were used in the case of open tubular coated columns [24,73], 5.5 mL $min^{-1}$ for lower molecular weight $N_2/O_2$ gaseous probes [78], and about 0.6 mL $min^{-1}$ for a monolithic column [71].

Prior to the measurements, the most fulfilling activation procedure of the studied material within the column is performed by heating the column to a suitably high temperature, using a slow ramp heating under a constant flow of the inert carrier gas overnight, that maintained the required thermal stability of the material.

Then, a trace amount of the probe molecules is then injected as a vapor phase. The adsorption data is collected under a wide range of temperatures, starting from room temperature up to 300 °C, depending on the nature of the adsorbed probes, with the retention time of the separated probes being the primary information collected during an IGC experiment.

### 3.1. HKUST-1

HKUST-1 (HKUST = Hong Kong University of Science and Technology), known also as MOF-199, was reported initially by Chui et al. [80]. This MOF entails copper(II)-dimer forming paddle-wheel SBUs, which form coordination bonds with four carboxylate groups from the organic linker trimesic acid (benzene-1,3,5-tricarboxylate (BTC)), and has the formula $Cu_3(BTC)_2 \cdot xH_2O$. The three-dimensional extension of these paddle-wheel units forms a three-dimensional structure with an underlying **tbo** topology (Figure 3). This MOF has a relatively high surface area in the range of 1500–2100 $m^2$ $g^{-1}$.

**Table 1.** The most significant applications of IGC for physicochemical characterization of MOFs.

| MOF Material | BET ($m^2\ g^{-1}$) | Pore Volume ($cm^3\ g^{-1}$) | Pore Opening (Å) | Pore Diameter (Å) | Utilized Probes | Key Parameters | Column Type | Column Dimension | Ref. |
|---|---|---|---|---|---|---|---|---|---|
| **HKUST (Hong Kong University of Science and Technology)** | | | | | | | | | |
| HKUST-1 | | | | | n-alkanes<br>Iso-alkanes | $K'$, $\Delta H_{ads}$ | Packed | 30 cm × 2.16 mm | [49] |
| HKUST-1 | 692.2 | 0.47 | | 12.1, 10.3, 4.7 | n-alkanes, Benzene<br>Cyclohexane, THF<br>Ethers | $\Delta H_{iso}$, $\Delta H_{ads}^{SP}$, $\Delta U_{diff}$, $\Delta G_{ads}$, $\Delta G_{interact}$, $\Delta G_{ads}^{SP}$, $\Delta G_{nonspec}$, $\Delta S_{ads}$, $\Delta S_{ads}^{SP}$, $K_A$, $K_D$ | WCOT | 3000 cm × 0.25 mm | [24] |
| HKUST-1<br>Fe-BTC | ~1800<br>~1450 | | | 10 | n-alkanes, BTX<br>Propane, Propylene | $\alpha$,$Q_d$ | Packed | 12 cm × 2 mm | [57] |
| HKUST-1<br>Fe-BTC | 1514<br>962 | 0.61<br>0.38 | | 9, 6 | n-heptane, Toluene<br>Methylcyclohexane | $\Delta H_{ads}$, $\Delta H_{imm}$, $\gamma_S^D$, $I_{sp}$ | Packed | 27 cm × 5.3 mm | [58] |
| HKUST-1<br>Fe-BTC | 1689<br>470 | | 6.9 | 4, 10, 11<br>25, 29 | n-alkanes Nitroalkanes | $K'$, $\Delta H_{ads}$, $\Delta S_{ads}$, $\Delta G_{ads}$, $\gamma_S^D$ | Packed | 10–15 cm × 2 mm | [38] |
| HKUST-1<br>Fe-BTC | | | | | n-alkanes, Benzene THF,<br>Acetone<br>Ethylether, EtAc | $K_A$, $K_D$ | Packed | 12 cm × 2 mm | [59] |
| **MIL (Matériaux de l'Institut Lavoisier)** | | | | | | | | | |
| MIL-47(V) | 750 | 0.32 | 8.5 | 8.5 | n-alkanes, Benzene<br>Iso-alkanes, Cyclohexane | $K'$, $\Delta H_{ads}$, $\Delta S_{ads}$, $\Delta G_{ads}$ | Packed | 30 cm × 2.16 mm | [60] |
| MIL-47(V) | | | | 7.9 × 12.0 | Benzenes<br>Heterocyclic | $K'$, $\Delta H_{ads}$ | Packed | 15 cm × 3.18 mm | [61] |
| Amino-MIL-53(Al) | 940–1038 | 0.50 | 8.5 | 8.5 | n-alkanes, 1-alkenes<br>Iso-alkanes<br>Benzene<br>Cyclohexane Cyclohexene | $K'$, $\Delta H_{ads}$ | Packed | 30 cm × 3.18 mm | [62] |
| $AlBDC_{Micro}$<br>$AlBDC_{Meso}$ | 1419<br>700 | 0.497<br>0.396 | | 8.6<br>25.8 | $CO_2/CH_4$<br>$CH_4/N_2$ | $\Delta H_{ads}$ | Packed | 40 cm × 3 mm | [63,64] |
| MIL-53 | 1169 | | 2.6 × 13.68.5 × 8.5 | | n-alkanes<br>Nitroalkanes | $K'$, $\Delta H_{ads}$, $\Delta S_{ads}$, $\Delta G_{ads}$, $\gamma_S^D$ | Packed | 10–15 cm × 2 mm | [38] |
| MIL-101(Cr) | 3054 & 4443 | 2.01 | 14.5 × 16 & ~12 | 29, 34 | n-alkanes, Toluene<br>p-xylene, Acetone | $\Delta G_{ads}^{SP}$ | Packed | 5 cm × 3 mm | [65] |

**Table 1.** *Cont.*

| MOF Material | BET ($m^2\ g^{-1}$) | Pore Volume ($cm^3\ g^{-1}$) | Pore Opening (Å) | Pore Diameter (Å) | Utilized Probes | Key Parameters | Column Type | Column Dimension | Ref. |
|---|---|---|---|---|---|---|---|---|---|
| **IRMOF (Isoreticular Metal-Organic Frameworks)** | | | | | | | | | |
| MOF-5<br>MOF-mono | 773<br>225 | | | 12<br>~7 | xylene isomers and EB | $\Delta H_{ads}$ | Packed | 80 cm × 1 mm | [66] |
| IRMOF-1-1<br>IRMOF-1-2<br>IRMOF-1-3 | 1161<br>781<br>208 | | 7.5 | 15 | More than 30 VOCs<br>n-alkanes | $\Delta H_{ads}$, $\Delta S_{ads}$, $\Delta G_{ads}$, $\gamma_S^D$, $\alpha_0$ | Packed | 2–3 cm × 0.53 mm | [67] |
| IRMOF-1<br>IRMOF-8<br>IRMOF-10 | 3046<br>1362<br>265 | | 10.9<br>12.5<br>16.7 | 24.9<br>41.9<br>132.6 | n-alkanes, Alkenes<br>Cycloalkane, Aromatics,<br>Chlorinated | $\Delta H_{ads}$, $\Delta S_{ads}$, $\Delta G_{ads}$, $\gamma_S^D$, $I_{sp}$ | Packed | 5 cm × 5.3 mm | [68] |
| **ZIF (Zeolitic imidazolate framework)** | | | | | | | | | |
| ZIF-8 | 1300–1800 | 0.592 | 3.4 | 11.4 | 13 VOCs<br>n-alkanes | $\Delta H_{ads}$, $\Delta S_{ads}$, $\Delta G_{ads}$, $\gamma_S^D$, $\alpha_0$ | Packed | 2–3 cm × 0.53 mm | [69] |
| ZIF-8 | | 0.66 | | 11.6 | EtOH/EtAc/water | $K'$, $\Delta H_{ads}$ | Packed | 5 cm × 1.59 mm | [70] |
| ZIF-8–(BuMA-co-EDMA) | 56 | | | | n-alkanes, Acetone<br>Diethylether,<br>DCM, EtAc, THF<br>Chloroform | $\Delta H_{ads}$, $\Delta S_{ads}$, $\Delta G_{ads}$, $\Delta G_{ads}^{SP}$, $\gamma_S^D$, $K_A$, $K_D$, $\chi$ | Monolith | 33.5 cm × 0.25 mm | [71] |
| ZIF-8 | 1766 | | 3.4 | 11.6 | n-alkanes, Nitroalkanes | $K'$, $\Delta H_{ads}$, $\Delta S_{ads}$, $\Delta G_{ads}$, $\gamma_S^D$ | Packed | 10–15 cm ×2 mm | [38] |
| ZIF-68 | | | | 11 × 16.5 | n-alkanes, 1-alkenes<br>Iso-alkanes<br>Cycloalkanes Aromatics<br>Polar probes | $K'$, $\Delta H_{ads}$ | Packed | 20 cm × 3.18 mm | [72] |
| **UiO-66 (Universitetet i Oslo)** | | | | | | | | | |
| UiO-66 | 614.3 | | 5–8 | 8–11 | Hex. Isomers Benzenes | $\Delta H_{ads}$ | WCOT | 2000 cm × 0.25 mm | [73] |
| UiO-66 | 614.3 | 0.24 | 7.5 | 11 | n-alkanes<br>Cyclohexane<br>Cycloheptane | $K'$, $\Delta H_{ads}$, $\Delta S_{ads}$ | Packed | 30 cm × 3.18 mm | [74] |
| UiO-66-Me,<br>UiO-66-$Me_2$,<br>UiO-66-$NO_2$ | 614.3 | | 5–8 | 8–11 | 70 VOCs<br>Alkanes, Alkenes<br>Aromatics | $K'$, $\Delta H_{ads}$, $\Delta S_{ads}$ | Packed | 35 cm × 3.18 mm | [75] |
| UiO-66,<br>UiO-66-Me,<br>UiO-66-$NO_2$ | | | | 17.5 and 11 | n-alkanes<br>Iso-alkanes | $K'$, $\Delta H_{ads}$, $\Delta S_{ads}$, $\Delta G_{ads}$ | Packed | 30 cm × 3.18 mm | [76] |

**Table 1.** *Cont.*

| MOF Material | BET ($m^2\ g^{-1}$) | Pore Volume ($cm^3\ g^{-1}$) | Pore Opening (Å) | Pore Diameter (Å) | Utilized Probes | Key Parameters | Column Type | Column Dimension | Ref. |
|---|---|---|---|---|---|---|---|---|---|
| **Miscellaneous MOFs** | | | | | | | | | |
| $SO_2$-DUT-5 | 1480 Langmuir | 0.47 | | 8.5–10.5 | n-alkanes, 1-alkenes Iso-alkanes Aromatic | $K'$, $\Delta H_{ads}$, $\Delta S_{ads}$ | Packed | 30 cm × 3.175 mm | [77] |
| $Cu(Qc)_2$ | 251.4 | 0.132 | | 4.7 × 6.6 | $O_2$ and $N_2$ | $\Delta G_{ads}$ | Packed | 30 cm × 3 mm ID | [78] |
| Y-fum-fcu-MOF | 835 | 0.35 | 4.7 | 5.8 Å and 7.6 | $C_4$ olefin isomers | $K'$, $\Delta H_{ads}$, $\Delta S_{ads}$ | Packed | 5 cm × 3.5 mm | [79] |

$\Delta U_{diff}$: differential energy of adsorption; $\Delta G_{interact}$: interaction Gibbs free energy of adsorption; $\Delta G_{nonspec}$: nonspecific interaction Gibbs free energy of adsorption; $\Delta H_{iso}$: isosteric enthalpy of adsorption; $\Delta H_{imm}$: enthalpy of immersion; *Isp*: Specific interaction parameter; $\alpha_0$: Deformation polarizability; $\alpha$: the separation factor; $Q_d$: equal to the enthalpy for the standard adsorbed state $\Delta H_{ads}$; SLS: stainless steel; WCOT: wall coated open tubular; VOCs: volatile organic compounds; BTX: benzene, toluene, xylene; ZIF-8–(BuMA-co-EDMA: ZIF-8-butyl methacrylate-co-ethylene dimethacrylate composite monolith.

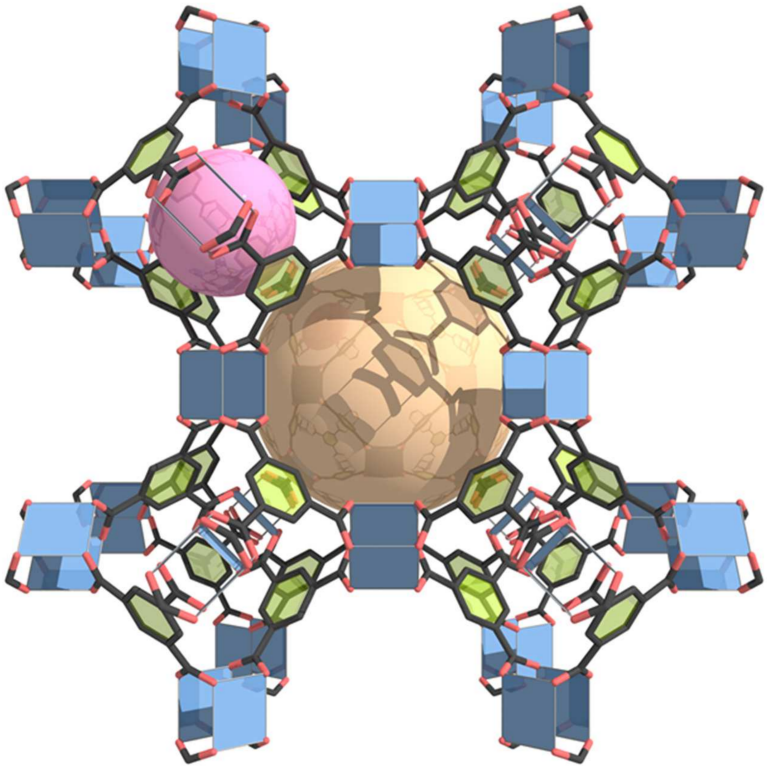


**Figure 3.** Crystal structure of the desolvated HKUST-1 ($Cu_3(BTC)_2$) MOF. The blue polyhedra represent the Cu paddlewheel SBU structure. (red: oxygen, and black: carbon).

Some research groups have identified this MOF as having three different types of cages with pore diameters of 4–4.7 Å, 10–10.3 Å, and 11–12.1 Å [81,82]. The large- and medium-sized pores are directly interconnected in an alternating manner, while the small 4–4.7 Å pores are situated at the vertexes of the large- and medium-sized pores and are directly interconnected with the large pores only.

Other authors have identified this MOF structures with only two types of pores: large 9–12 Å pores connected by 7–8.3 Å windows, and small 5 Å pores accessible by 3.5 Å windows [80,83,84]. In the hydrated HKUST-1 structure, a water molecule is coordinated at the axial position of the paddlewheel unit and can be removed upon an activation process, without any change in MOF crystallinity or loss of porosity. An unoccupied coordination site at the $Cu^{2+}$ atoms is called a coordinatively unsaturated site (CUS) and can be accessed by other probe molecules [82]. One metal ion coordination site is unsaturated and therefore open to Lewis basic molecules [80,85]. HKUST-1 possesses Lewis acidic centers from the copper(II)-SBUs, and Lewis basic centers from $\pi$ electron-rich benzene rings in the BTC molecule.

The Fe-BTC MOF is analogous in structure to HKUST-1 and is synthesized as a porous solid, however, in a gel-like form (surface area is about 1300–1600 $m^2\ g^{-1}$) [86]. Fe-BTC MOF, unlike HKUST-1, has not been thoroughly explored or studied because its structure is not highly crystalline that may cause distortion of its pore geometry. Its morphological properties were studied in comparison to MIL-100 (Fe) (MIL = Material of Institute Lavoisier) [87], and Fe-BTC MOF has been found to encompass 21.2% of $Fe^{3+}$ as a nodal metal and the BTC linker in a distorted form of MIL-100(Fe) MOF [87,88]. While its composition is similar to that of MIL-100 (Fe), with respect to many applications, Fe-BTC MOF cannot be compared directly with MIL-100 (Fe). HKUST-1 and Fe-BTC MOF were commercialized under the commercial names Basolite C300 and F300, respectively.

Finsy et al. [49] demonstrated a possible use of HKUST-1 MOF for adsorptive separation based on shape selectivity. They found that linear alkanes were adsorbed preferably over methyl-branched alkanes. The high adsorption enthalpy and low Henry constants of

the branched alkanes relative to those of their linear isomers suggested shape selectivity, as the Henry constants decreased with branching degree.

Shape-based discrimination was used to examine the logarithm of the vapor pressure versus the logarithm of the Henry constant plot (Figure 4). A linear relationship with 2-methyl-branched alkanes on this trend line was observed for linear alkanes, although not all alkanes branched like 3-methyl- and dimethyl- alkanes behaved similarly. This suggests that HKUST-1 cannot be efficiently used for separating linear alkanes from 2-methyl-branched alkanes based on their shape, but it can separate linear alkanes from 3-methyl and dimethyl-branched alkanes.

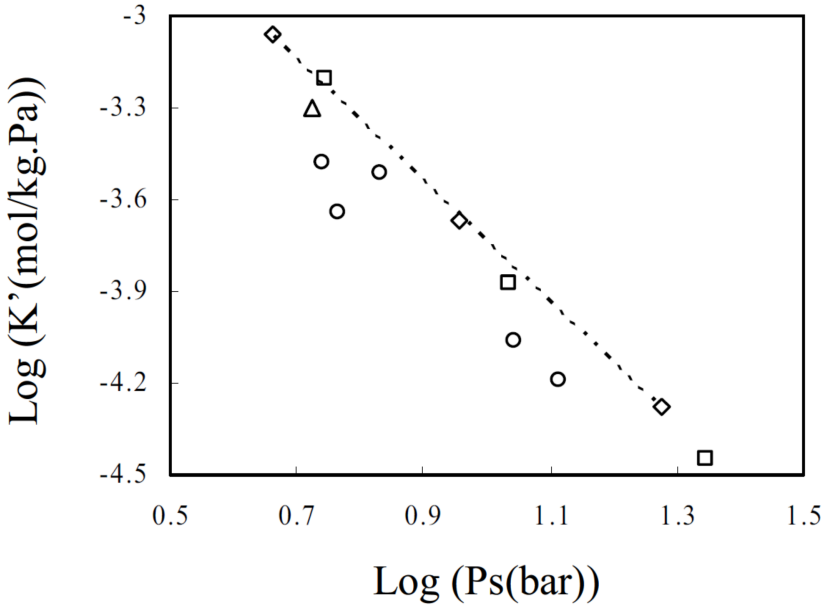



**Figure 4.** Logarithm of the Henry constants of linear (◊), 2-methylbranched (□), 3-methyl-branched (Δ) and dimethyl-branched alkanes (o), calculated from the measured chromatograms at 160 °C, versus the logarithm of their saturated vapor pressure at 160 °C. Reprinted with permission from [49]. Copyright (2007) Elsevier.

Münch and Mertens [24] applied the IGC method to evaluate the donor properties of the HKUST-1 linker BTC and the acceptor properties of the CUS sites. These experiments were executed using a GC wall-coated silica capillary column of 30 m length and 0.25 mm inner diameter, unlike the majority of IGC studies, which typically utilize a short-packed column (Table 1) [24].

The chromatogram indicates that benzene showed a longer retention time than cyclohexane (Figure 5), but a lower boiling point. This suggests the existence of specific interactions, for example, π–π interactions between the benzene ring π-electrons of the BTC linker in HKUST-1 and the π-electrons in the benzene moiety of the analyte. Benzene also showed a higher value of $\Delta H_{ads}$ than cyclohexane, implying a stronger interaction. A thermodynamic investigation of a group of ethers with different branches, including THF (Figure 5), revealed a significant effect of the geometry of the analytes on adsorption. It was concluded that there was a combination of two factors: open metal site accessibility, which allowed interaction with oxygen free electron pairs; and an entropic effect caused by the degrees of freedom of the alkyl chains [24].

The Gutmann donor and acceptor numbers of a particular probe analyte permitted a quantifiable assessment of the Lewis acidity and basicity sites in the HKUST-1 structure. The HKUST-1 acceptor properties had a value of 1.6 for $K_A$, and the surface donor properties had a value of 0.4 for $K_B$. From these numbers, it was concluded that HKUST-1 can be categorized as primarily Lewis acidic, which is attributed to the prevalence of CUS [24].

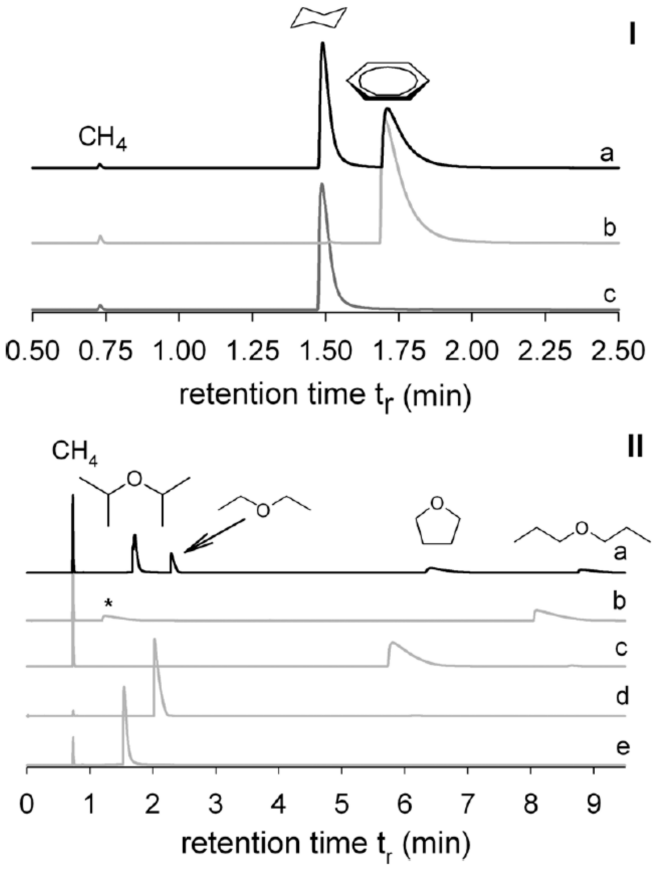



**Figure 5.** (**I**) Chromatographic separation of a mixture of methane (for the determination of the dead time in all chromatograms), cyclohexane, and benzene (a) pure benzene (b), and of pure cyclohexane (c). Experimental setup: column: HKUST-1@$SiO_2$ (30 m × 0.25 mm × 0.15 µm); carrier: He, flow: 4.37 mL $min^{-1}$, 76.2 cm $s^{-1}$; oven: 473.15 K, isotherm; injector: split, 11.7:1 at 250 °C; detector: FID at 250 °C. (**II**) Chromatographic separation of a mixture of methane, diisopropyl ether, diethyl ether, tetrahydrofuran, and di-n-propyl ether (black line) (a). Chromatograms of pure substances except methane. (b) Di-n-propyl ether. (c) Tetrahydrofuran. (d) Diethyl ether. (e) Diisopropyl ether. Experimental setup: column: HKUST-1@$SiO_2$ (30 m × 0.25 mm × 0.15 µm); carrier: He, flow: 4.14 mL $min^{-1}$, 72.5 cm $s^{-1}$; oven: 523.15 K, isotherm; injector: split, 12:1 at 250 °C; detector: FID at 250 °C. (*—impurity) [24]. Published by The Royal Society of Chemistry.

In another study by Autie-Castro et al. [59], n-butylamine thermodesorption analyses were performed using IGC to compare HKUST-1 to its analog Fe-BTC with respect to their acid–base properties. Samples of the proposed materials were saturated with n-butylamine to quantify both sites (acidic and basic) from the desorption curves of n-butylamine using the n-butylamine thermodesorption technique.

The IGC measurements yielded 0.81 and 0.60 as the acidity constants ($K_A$) and 0.09 and 0.28 as the basicity constants ($K_B$) for Fe-BTC and HKUST-1, respectively. Moreover, the n-butylamine thermodesorption study indicated a total acidity of 2.06 mmol $g^{-1}$ for Fe-BTC and 0.49 mmol $g^{-1}$ for HKUST-1. This behavior may be attributed to the superior polarizing rule of $Fe^{3+}$ compared to $Cu^{2+}$ due to the higher charge. As a result, both MOFs, HKUST-1 and Fe-BTC, were verified as being predominantly Lewis acidic.

Specific interaction contribution values of 4.1 and 3.2 kJ $mol^{-1}$ at 200 °C were acquired for the benzene moiety in HKUST-1 and Fe-BTC, respectively. Furthermore, the contributions of the specific interactions regarding THF at 200 °C were found to be 14.5 kJ $mol^{-1}$ for HKUST-1 and 17.9 kJ $mol^{-1}$ for Fe-BTC. HKUST-1 has a mildly basic surface character, whereas Fe-BTC has a more prominent acidic character, resulting in more benzene (acidic)

interactions on the HKUST-1 material surface and more THF (basic) interactions on the Fe-BTC material surface.

Autie-Castro et al. [57] measured the $\Delta H_{ads}$ on both Fe-BTC and HKUST-1 for n-alkanes, propane, propylene, benzene, toluene, and xylene. Dispersive interactions were the dominant adsorption mechanism for n-alkanes, and $\Delta H_{ads}$ was found to increase with the number of carbon atoms. The electrostatic interaction of propylene and aromatics through its dipole and/or quadrupole moments via the guest-host π–π coupling led to a higher $\Delta H_{ads}$ value for propylene than propane.

Higher $\Delta H_{ads}$ values were found for HKUST-1 than Fe-BTC, due to the ordered crystal structure and molecular ease of access to the porous structure of HKUST-1. In the case Fe-BTC, which has does not have a well-defined crystal structure, local deformations of its flexible organic ligand may account for the restricted accessibility of pocket-type pores, where small probe molecules were restrained in a small volume and thus contributed more to the adsorption forces of dispersive interactions.

Gutiérrez et al. [58] compared HKUST-1 and Fe-BTC in more depth by comparing the $\Delta H_{ads}$ obtained from IGC and the $\Delta H_{imm}$ (the enthalpy of immersion) obtained from immersion calorimetry. For the three studied adsorbates (n-heptane (HEP), methylcyclohexane (MCH), and toluene (TOL)), the interaction strength was higher for Fe-BTC than HKUST-1. This was a result of the better accessibility to the active sites in Fe-BTC, as it has a lower fraction of microporous surface area. Although Fe-BTC does not have a specified crystalline structure, the open metal sites can favor electrostatic interactions with the adsorbates, leading to an increase in the overall affinity of the interaction.

The $\Delta H_{imm}$ followed the same order as the enthalpy of adsorption, i.e., TOL > HEP > MCH, and was consistent with the $\Delta H_{ads}$ measurements for HKUST-1 (Figure 6). However, unlike $\Delta H_{ads}$, the $\Delta H_{imm}$ values for Fe-BTC were in the inverse order with respect to the smallest size of the adsorbates: TOL (4.012) < HEP (4.014) < MCH (4.982) (Figure 7) [89]. This suggests that these electrostatic interactions are less crucial and the accessibility of the adsorbates to the pores is more relevant.

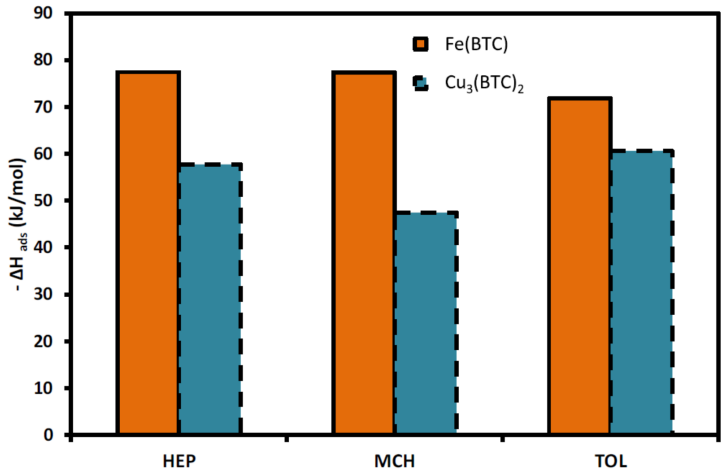



**Figure 6.** Enthalpy of adsorption for Fe-BTC and HKUST-1 for the three adsorbates. Reprinted with permission from [58]. Copyright (2015) Elsevier.

The higher cross-section area of the adsorbent n-alkanes on the surface of both MOFs makes the dispersive interaction of the surface energy produced more prominent for HKUST-1 than for Fe-BTC. Additionally, the highest specificity of the interaction was also reported on HKUST-1, which is contrary to what was expected, as indicated by the specific interaction parameter ($I_{sp}$), which reflects on the surface acid–base nature.

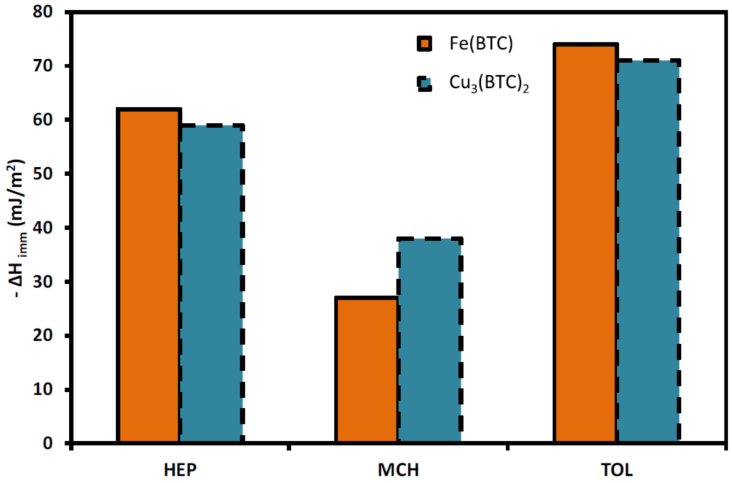



**Figure 7.** Enthalpy of immersion for Fe-BTC and HKUST-1 for the three adsorbates. Reprinted with permission from [58]. Copyright (2015) Elsevier.

Another research group [38] utilized IGC as a prescreening tool. They effectively examined the affinity of MOFs for targeted probes in the gas phase. For the commercially available MOFs, like HKUST-1 (Basolite C300), Fe-BTC (Basolite F300), MIL-53 (Basolite A100), and ZIF-8 (Basolite Z1200), a preconcentration process for sensitive sensing of nitroalkanes was developed, and the results were associated to those of the Tenax TA porous archetype.

In this study, HKUST-1 showed an enrichment factor 109-fold higher than that of Tenax, as revealed by the high value of $\Delta H_{ads}$ for nitromethane (Figure 8), and a dispersive element of surface energy values ($\gamma_S^D$) above 100 mJ m$^{-2}$. As predicted, the enthalpy of adsorption values for nitroalkanes on HKUST-1 (relatively basic) were higher than those on Fe-BTC (Figure 8) since the nitroalkanes were slightly acidic due to the electron-withdrawing effect of nitro groups.

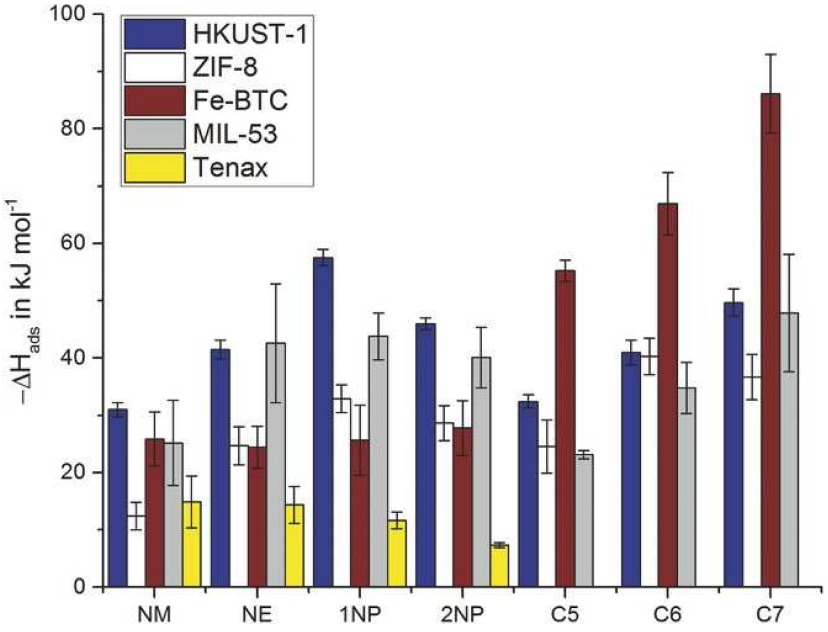



**Figure 8.** Enthalpies of adsorption for regular and nitroalkanes on all sorbents investigated in this study. Enthalpies in kJ mol$^{-1}$. Analytes: nitromethane (NM), nitroethane (NE), 1- and 2-nitropropane (1NP and 2NP), as well as pentane (C5), hexane (C6), and heptane (C7). Reprinted with permission from [38]. Copyright (2018) Elsevier.

To correlate IGC measurements to a frontal technique, the results of IGC experiments were compared to micro-breakthrough ones with downstream thermal desorption experiments. HKUST-1 also displayed impressive improvement factors above 2000 while sampling at a nitromethane source of 1000 ppm.

### *3.2. MIL-Based MOFs*

MIL-47 is a rigid MOF composed of infinite chains of $VO_6$ octahedra connected via the dicarboxylate groups of terephthalate organic ($H_2BDC$) ligands. In this structure, a microporous framework is created having one-dimensional diamond-shaped channels with pore apertures of 7.9 Å × 12.0 Å (Figure 9) [90].

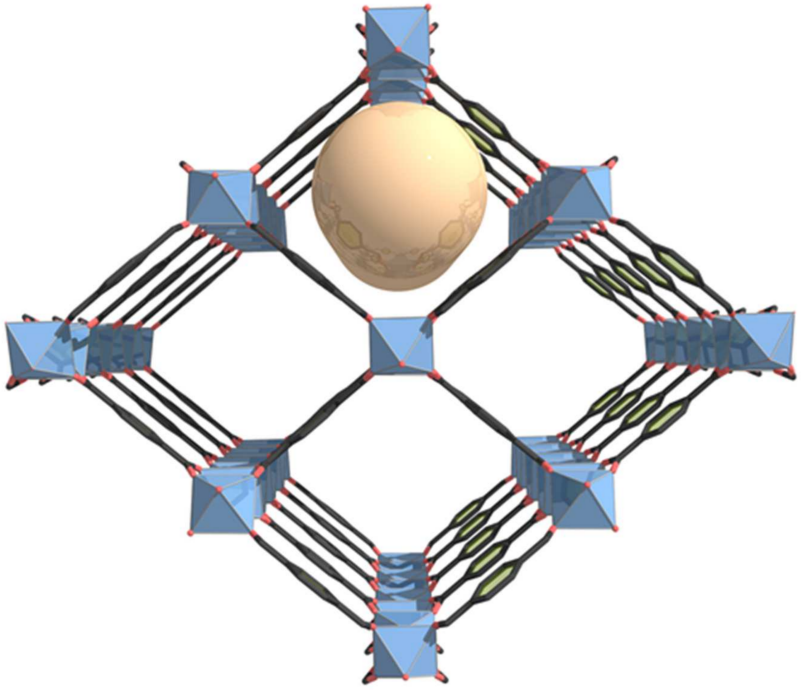


**Figure 9.** Crystal structure of MIL-47(V) with a view along the chain axis, highlighting the 1D pores system. The blue polyhedra represent the $V^{4+}O^6$ ocahedral shared in the chain. (Red: oxygen, and black: carbon).

The adsorption properties of MIL-47(V) were evaluated by Finsy et al. [60] in a combined IGC experimental and Monte Carlo simulation study. Their report showed that both linear and branched alkanes can adsorb into the pores of MIL-47(V) without any steric hindrance. The dependency of adsorption enthalpy and the Henry constants on the carbon number was significantly correlated between the simulations and experiments. n-Hexane (50.6 kJ $mol^{-1}$) was adsorbed more strongly than benzene (43.4 kJ $mol^{-1}$) and cyclohexane (45.2 kJ $mol^{-1}$) because it has more hydrogen atoms. The adsorption energies of the studied nonpolar molecules were governed by van der Waals interactions, and the adsorption of the benzene probe molecules was further affected by Coulombic interactions.

Similar work on MIL-47(V) to evaluate its physicochemical properties via IGC was done on the adsorption of substituted aromatics in addition to other heterocyclic molecules [61]. Quantitative structure−property relationships (QSPRs) between the adsorption and molecular properties were established using principal component analysis and partial least-squares regression. With respect to heterofunctionalized probes, the adsorption properties tended to associate with the polarization and/or electronegativity of the substituent. The effect of the resulting dipole moment originating from the substituent placing was observed [61].

The experimental results indicated that the molecular polarizability of the halogen series perfectly fell on the alkyl aromatics series (Figure 10), suggesting that the observed

properties were likely due to increased polarization and not to higher electronegativity of the halogen atoms. The oxygen-containing functional groups like nitro, methyl ester, and carbonyl were removed from this pattern. Thus, the expanded π-system enabled further delocalization of π-electrons from the substituent and the aromatic ring. Consequently, the electron-rich substituent attached more tightly to the MOF material than the alkyl fragments.

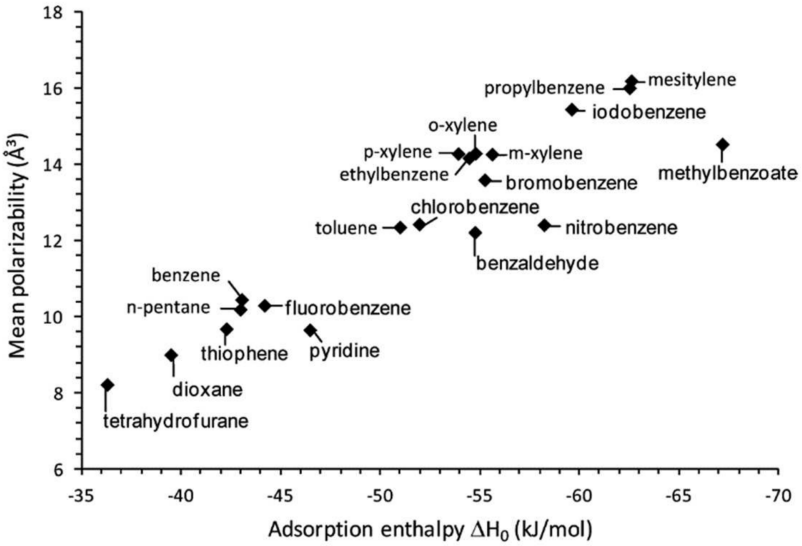



**Figure 10.** Relationship between mean molecular polarizability and adsorption enthalpy at zero coverage. Reprinted with permission from [61]. Copyright (2012) American Chemical Society.

Flexible MOFs are a special class of MOF materials that can reversibly alter their framework when guest molecules are introduced or removed. This leads to unique properties such as the breathing effect and the gate-opening phenomenon, in which pores contract or extend during adsorption [91–93]. Examples of breathing materials are MIL-53 [94] and its functional derivatives [91,95–97]. MIL-53 is constructed from $MO_4(OH)_2$ octahedra (where M can be $Fe^{3+}$, $Cr^{3+}$, or $Al^{3+}$) with 1,4-terephthalate (BDC) as the linker. In this way, MIL-53, which is also known under the commercial name Basolite A100, is a crystalline material having one-dimensional diamond-shaped pores with an 8.6 Å free diameter [91,98].

Couck et al. [62] utilized IGC to study the adsorption properties of amino-MIL-53 (Al). Amino-MIL-53 (Al) also has one-dimensional channels, similar to the amino-free MIL-53 analog, with a pore diameter of nearly 7.5 Å. The amino groups are directly inside the pores as a result of using 2-amino terephthalic acid as a linker rather than terephthalic acid [99], which leads to an enhanced affinity towards $CO_2$ [95].

Couck et al. found that the adsorption enthalpy and Henry's adsorption constants of iso-alkanes were considerably smaller than those of linear alkanes, highlighting the shape selectivity features of amino-MIL-53. Furthermore, the amino groups exposed in the pores of amino-MIL-53 enhance the electrostatic contribution of molecules with double bonds. Although double bonds contribute to total interactions, van der Waals interactions were found to be the dominant element for the adsorption interactions of molecules. Using a simple model, Couck et al. predicted that hydrogen atoms and double bonds contributed to these adsorption properties. The determined confinement factor Z pointed to an increased degree of confinement in amino-MIL-53(Al) compared to MIL-53 and MIL-47. Amino-MIL-53(Al) also exhibited a smaller pore aperture, which is due to either the presence of amino groups or to the framework shrinking as a result of the interaction between amino functional groups and hydroxyl groups.

Sun et al. demonstrated that the enhanced adsorption activities of $CO_2$ over $CH_4$ [63] and $CH_4$ over $N_2$ [64] over Al-BDC MOFs due to larger pore size. Their XRD patterns were different from those of MIL-53(Al). There was a slight difference compared with the

standard MIL-53(Al), which may be as a result of the presence of some free $H_2BDC$ linkers within the pores and the metastable phase of BDC and $Al^{3+}$ as a result of the different conditions of crystal growth. The pore size of Al-BDC MOFs increased from 0.86 ($AlBDC_{Micro}$) to 2.58 nm ($AlBDC_{Meso}$) via a simple washing and drying process. Subsequently, an analysis of the adsorption equilibrium and thermodynamics of the different gases, $CH_4$, $CO_2$, and $N_2$, was done via volumetric−chromatographic and IGC methods [62].

The initial adsorption heat was estimated to be 11.5 kJ $mol^{-1}$ for $CH_4$ and 25.2 for $CO_2$ on $AlBDC_{Meso}$ MOF, which is approximately 25% less than on $AlBDC_{Micro}$ MOF. These data indicated that enlarged pore size not only increased the $CO_2$ adsorption selectivity over that of $CH_4$, but also decreased the value of $\Delta H_{ads}$, suggesting that it should be the preferred method for selecting a satisfactory absorbent for $CO_2/CH_4$ separation [63]. The heats of adsorption of $CH_4$, $N_2$, and $CO_2$ were calculated as 15.3, 11.5, and 32.2 kJ $mol^{-1}$, respectively, which is aligned with the gravimetric study [64].

MIL-101(Cr) with the formula ($Cr_3O(H_2O)_2F(BDC)_3$) has a very large surface area and cubic cell volume with two kinds of cages: smaller 29 Å cages with pentagonal faces and larger 34 Å cages with both pentagonal and hexagonal faces [100]. The adsorption behavior of MIL-101(Cr) towards p-xylene was investigated using IGC [65]. These data showed that the specific component of the free energy of adsorption ($\Delta G_{spec}$) values of the polar probes were negative, suggesting spontaneous adsorption. The adsorption specific component of the free energy $\Delta G_{spec}$ for polar molecules on MIL-101(Cr) were found to be in the order p-xylene > toluene > acetone. The $\Delta G_{spec}$ for polar probes was inversely proportional to their dipole moment, although the authors have not provided an explanation for this phenomenon [65].

### *3.3. Isoreticular Metal-Organic Frameworks (IRMOF)*

The IRMOF structure consists of $Zn_4O$ tetranuclear clusters linked by various rigid linear ditopic linkers, giving the obtained frameworks different pore aperture sizes and forming a cubic structure with connected channels (Figure 11) [101].

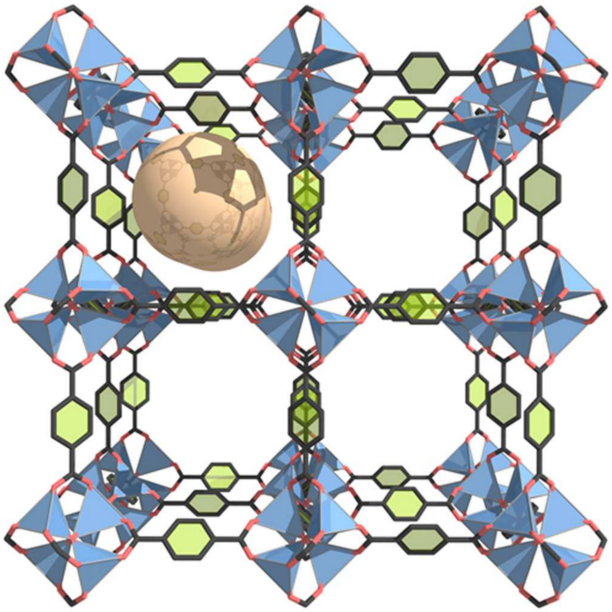


**Figure 11.** Crystal structure of IRMOF-1 (MOF-5), with the formula $Zn_4O(BDC)_3$, where BDC = 1,4-benzodicarboxylate, and blue tetrahedrons represent the $Zn_4O(\text{-}CO_2)_6$ SBU from coordination of BDC to the zinc center. (Oxygen; red, and black: carbon).

The diffusion and adsorption of xylene isomers as well as ethylbenzene (EB) on IRMOF-1 (MOF-5) ($[Zn_4O(BDC)_3]_n \cdot mDMF$) [102] and MOF-monoclinic ($[Zn_3(BDC)_3(H_2O)_3(DMF)_4]_n$) [103] were studied using IGC, breakthrough adsorption, and static vapor-phase adsorption [66].

IRMOF-1 and MOF-monoclinic have been shown to have different selectivity for the separation of the studied probes. On IRMOF-1, EB was found to be eluted first; however, xylene isomers were eluted similarly. The equilibrium constants controlled the elution order of the xylenes and EB on IRMOF-1. On the other hand, MOF-monoclinic exhibited a preferable adsorption for the p-xylene isomer, which was believed to result from some hindrance due to pore size that governed the diffusion of the isomers in the MOF micropores.

The McReynolds constants of IRMOF-1 showed that the nonpolar nature of that material was advantageous for the thermodynamic separation of the xylene and EB isomers. The intermediate polarity of MOF-monoclinic was attributed to the higher accessibility of its SBUs to isomers, and its pore shape was found to play a more significant role in separation than in IRMOF-1.

The properties of IRMOF-1 can change markedly based on its synthesis, activation method, and contact with atmospheric humidity [104–107]. Different IRMOF-1 samples prepared with different synthetic schemes were used to examine the impact of structural decomposition on adsorption behavior [67]. The infinite-dilution assumption in the adsorption isotherm linear segment was confirmed as valid through the independence of the chromatographic peak retention times for nonpolar n-alkanes with respect to concentration. On the other hand, the compounds having considerable hydrogen-bond basicity groups, such as diethyl ether, acetone, ethyl acetates and THF, were observed to vary from this ideal behavior.

The independence of the amended retention volume from the flow rate showed that the mass transfer did not affect the retention time. This implies that the amended retention volumes and all related calculated values indicate equilibrium behavior. The calculated values for enthalpy and entropy were more significant than those predicted by Monte Carlo simulations [108]. The presence of a nonporous phase in IRMOF-1 appeared to result in active sites with higher energies than those existing in standard IRMOF-1. The obtained linear relationships amongst the carbon number, the enthalpy of adsorption, and the free energy of adsorption were attributed to the additive nature of dispersive interactions.

The dispersive component of the surface energy ($\gamma_S^D$) values for IRMOF-1 samples was calculated to be between 48 and 91 mJ $m^{-2}$, which is noticeably lower than the values for zeolites and activated carbons, which have been frequently recorded in the range of 200–500 mJ $m^{-2}$ [51,109–111]. This indicated a comparatively inactive surface for IRMOF-1, which was believed to be due to its large cages. Most of the interactions between the n-alkanes and the organic part of the framework were due to steric constraints near the metallic corners and the size of the n-alkanes. The deformation polarizability was much better suited to measuring negative values for free adsorption energy than for vapor pressure (Figure 12). Most of the data points outside of the nonpolar line were related to the strong alkali and chlorinated molecules. From this fact and the observation that all the aromatics tended to lie on the nonpolar line, it was concluded that the basicity component of adsorption of the hydrogen bond prevailed for IRMOF-1. Similarly, the influence of the π-bond polarizability seems to be less significant [67].

In another study, Gutiérrez et al. [68] evaluated the interaction of some volatile organic compounds (VOCs) with three IRMOFs (IRMOF-1, IRMOF-8, and IRMOF-10) using IGC in order to assess the adsorption and link it to the morphological structure. The organic linkers of the three MOFs are terephthalic acid (IRMOF-1); 2,6-napthalene dicarboxylic acid (IRMOF-8); and 4,4-diphenyl dicarboxylic acid (IRMOF-10). Thus, they vary only in pore size. Overall, the strength of adsorption was enhanced in the presence of lattice defects and increasing numbers of carbon atoms in the organic linkers; accordingly, IRMOF-10 had the strongest interaction with the VOCs, followed by IRMOF-8 and finally IRMOF-1. Gutiérrez et al. deduced that the dispersive component of the surface free energy and the thermodynamic compensation effect of the n-alkanes exhibited the same centers of adsorption on all three MOFs. Furthermore, they witnessed that the existence of π electron-rich aromatic rings or double bonds tended to increase the specific interaction element through a preferred interaction with the aromatic rings. Consequently, the specificity of

the interactions was connected to the chemistry of the organic ligands rather than to the structure.

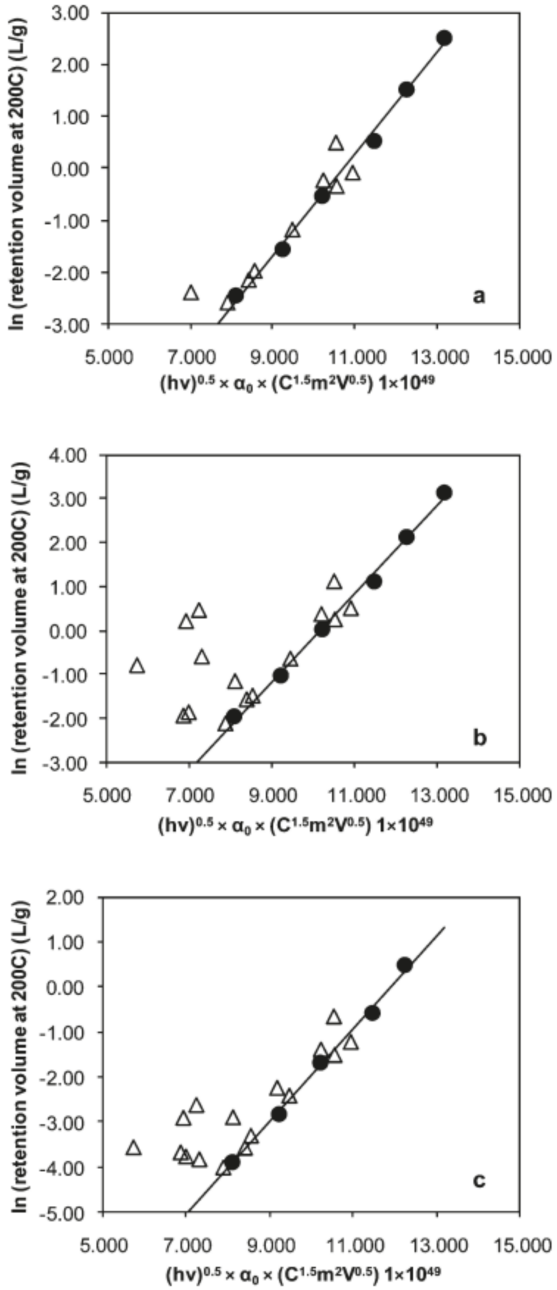



**Figure 12.** Correlation between a VOC deformation polarizability and the free energy of adsorption (retention volume) at 200 °C as measured by IGC shown for (**a**) IRMOF-1 sample 1; (**b**) IRMOF-1 sample 2, and (**c**) IRMOF-1 sample 3. In these plots, the solid circles represent the series of n-alkanes, and the triangles represent other measured analytes. Reprinted with permission from [67]. Copyright (2010) American Chemical Society.

### *3.4. Zeolitic Imidazole Frameworks (ZIFs)*

ZIFs have isomorphic topologically with zeolites. They are composed of tetrahedrally linked transition metal ions like zinc, cobalt, etc., that are coordinated by imidazolate-based ligands. The metal-imidazole-metal angle is 145°, which is analogous to the Si-O-Si angle present in zeolites. ZIF-8 is one of the most utilized members of this family, consisting of 2-methylimidazole ligands connected with $Zn^{2+}$ ions to form eight sodalite (**sod**) cages that

construct an overall cubic structure (Figure 13). ZIF-8 has been commercialized under the commercial name Basolite Z1200.

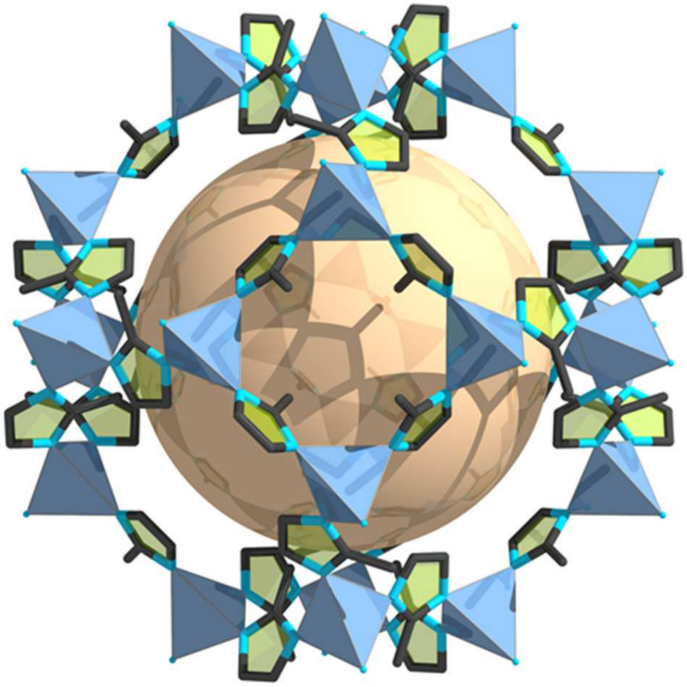


**Figure 13.** Crystal structure of ZIF-8 with the underlying **sod** topology, where blue tetrahedra indicate the $ZnN_4$ SBUs. (Blue: nitrogen, and black: carbon).

Luebbers et al. [69] applied IGC to investigate the adsorption behavior of many gases and VOCs on ZIF-8. Such highly halogenated compounds, branched alkanes, and aromatic compounds eluted rapidly with small tailing peaks and retention times, demonstrating a molecular sieving behavior that inhibited them from accessing the narrow windows of the MOF structure. On the other hand, the retention behavior of many of the studied compounds, especially n-alkanes, implied an unexpected flexibility of the ZIF-8 structure, even with n-alkanes with kinetic diameters similar or larger than 0.43 nm [112], significantly larger than the recorded ZIF-8 pore window size of 0.34 nm [113,114].

Owing to the mainly organic character of the reachable binding sites, ZIF-8 exhibited a lower surface energy than several other MOFs and microporous materials [113]. H-bond interactions were considered a dominant factor, as in the case of acids, amines, and alcohols that bind too strongly to be adequately studied in this method. Nevertheless, the adsorption of other probes, such as ketones, tends to be far less effective owing to the absence of such strong acid sites. Additionally, electrostatic interactions were essential, as the definite component of the adsorption free energy was observed to be significantly linked to the dipole moments of the adsorbates. In addition, a major increase in the adsorption of alkenes over alkanes was found to originate from the polarizability of the $\pi$-electrons, in addition to the interactions resulting from the induced dipole with the ZIF-8 structure.

The molecular sieving behavior and adsorption properties of ZIF-8 were also highlighted by Yusuf et al. [71,115]. They examined the impact of integrating various percentages of ZIF-8 into a BuMA-co-EDMA (butyl methacrylate-co-ethylene dimethacrylate) monolithic capillary column. The adsorption enthalpy values of both the neat monolith and the ZIF-8@(BuMA-co-EDMA) composite monolith did not reach the limit of physical and chemical adsorption (62.8 kJ $mol^{-1}$) [116], suggesting the presence of only physical alkane interactions. The proximity to the heat of liquefaction for n-alkanes [117] and its change in enthalpy of adsorption showed that secondary weak intermolecular forces dominate the interactions through the monolith-n-alkane interface [118]. The addition of ZIF-8 particles to the monolithic organic material increased the dispersive element of the surface energy

($\gamma_S^D$) values, revealing a more energetic surface. A Lewis basic character with $K_B/K_A > 1$ (but with a higher basicity for the neat monolith) was reported based on the results of the $K_B/K_A$ ratios for both materials and suggests an acidic character for ZIF-8 [71].

In another study [70], the adsorption and separation of ethanol/ethyl acetate (EA)/water mixtures, formed during an industrial process for the synthesis of EA, were studied on ZIF-8. Single- and multicomponent isotherms of adsorption, acquired via gravimetric and breakthrough experiments, showed high adsorption ability and selectivity to EA. The higher interaction strength between EA and ZIF-8 was verified by IGC experiments. At zero coverage, the EA adsorption enthalpy was equivalent to 38.6 kJ $mol^{-1}$, while ethanol sorption released less energy (23.4 kJ $mol^{-1}$). The larger polarizability of $\pi$-electrons containing ester carbonyl groups than hydroxyl groups may further enhance adsorption [119].

ZIF-68, which has a **gme** topology, consists of $ZnN_4$ tetrahedra connected by two derivatives of imidazole linkers; the first is a polar 2-nitroimidazolate linker, and the second is a nonpolar benzimidazolate linker, in a 1:1 ratio. ZIF-68 consists of two diverse channels and three types of cages, which are large, medium, and small [120]. A six-membered channel (diameter approximately 3.4–3.8 Å) forms alternating small and medium cages, where nitro groups are projected within the cages, maintaining the polar character. The larger channel (12-membered with a diameter of approximately 7.5–8.6 Å) is predominantly constructed from imidazole linkers substituted with benzene, resulting in this channel's pronounced nonpolar character. Since the large cages occupy 74% of the total volume, ZIF-68 was assigned an overall nonpolar behavior [121].

An IGC investigation of ZIF-68 [72] demonstrated a lack of shape-selective behavior with the complex pore structure of this material. The logarithm of the Henry constant was plotted as a function of the logarithm of vapor pressure for n-alkanes and isoalkanes to evaluate the shape selectivity (Figure 14). The same linear correlation for linear and branched alkanes indicated the absence of shape selectivity [122,123]. The zero-coverage adsorption enthalpies of the branched alkanes were approximately 5−8 kJ $mol^{-1}$ lower than those of the linear chains. This is typical of materials that are not shape selective. The structure demonstrated an overall nonpolar framework with limited polar centers. In contrast to alkanes, alkenes, and aromatics, small polar probes exhibited relatively high adsorption enthalpies. Due to the presence of nitro moieties, the cages in the small channel served as favorable adsorption positions for such polar molecules.

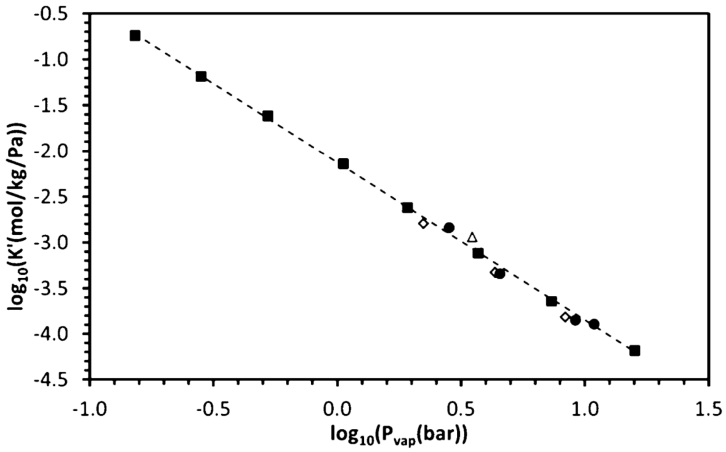



**Figure 14.** Logarithm of Henry constants as a function of the logarithm of the vapor pressure at 423 K for linear (■), monomethylbranched (◇), dimethylbranched (●), and trimethylbranched (Δ) alkanes on ZIF-68. Reprinted with permission from [72]. Copyright (2015) American Chemical Society.

### *3.5. UiO-66 MOF*

UiO-66 MOF (UiO = Universitetet i Oslo) is a zirconium-based MOF composed of hexamers of eight coordinated $ZrO_6(OH)_2$ polyhedra and BDC linkers [124]. UiO-66 has

an **fcu** topology, with a rigid cubic three-dimensional structure comprised of octahedral and tetrahedral cages with diameters of 11 and 8 Å, respectively. The cages are accessed solely via the triangular pore windows of approximately 5–7 Å (Figure 15).

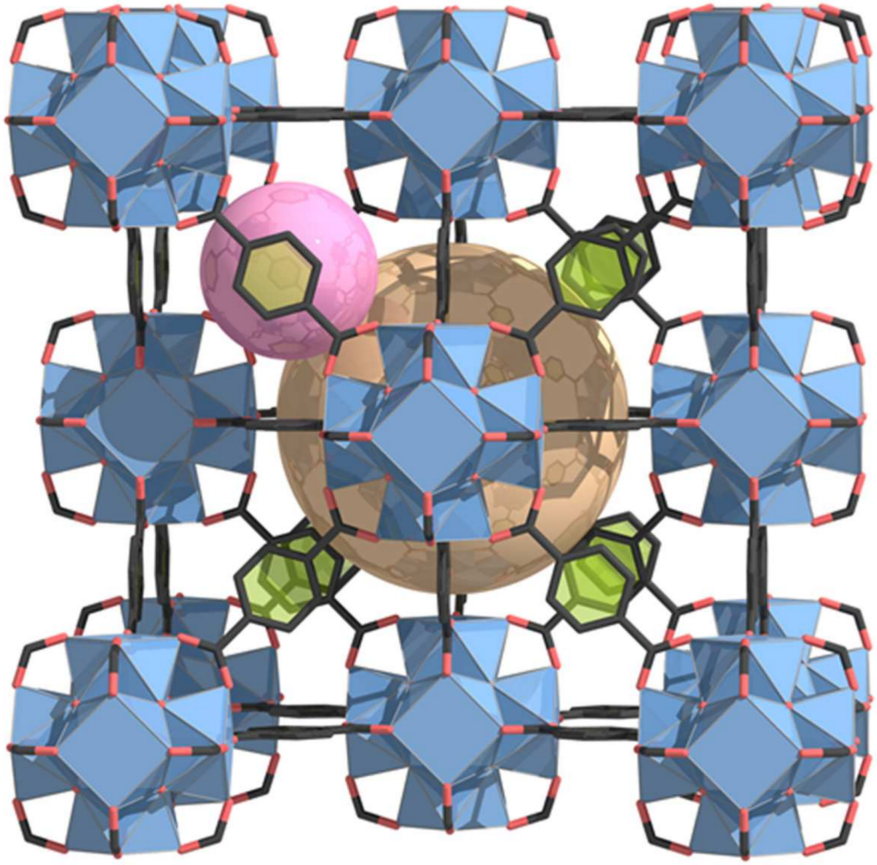


**Figure 15.** Crystal structure of UiO-66 MOF, where blue polyhedra represent the 12-coordinated Zr-based metal clusters that are interconnected by BDC linkers with **fcu** topology. (Red: oxygen, and carbon: grey; pink sphere represents the tetrahedral cage and brown sphere represents the octahedral cage).

UiO-66 is considered one of the first MOFs that showed reverse shape-selectivity separation properties [125]. In a regular shape-selective material, a molecule having a more compact size with respect to its molecular weight will adsorb preferentially. Probes with higher boiling points and comparable chemical compositions will selectively adsorb on nonselective surfaces over lower-boiling molecules.

Chang et al. [73] demonstrated that a UiO-66-coated capillary column showed both a molecular sieving effect and a reverse shape selectivity. This capillary column favored adsorption of branched alkanes over their linear analogs, thus demonstrating reverse shape selectivity. This column also showed that branched hexane isomers had higher adsorption enthalpies than hexane, indicating stronger interaction with branched alkanes. However, the retention time of the bulkier 1,3,5-trimethylbenzene was smaller than that of n-propyl- and iso-propylbenzene, exhibiting a molecular sieving effect (Figure 16). Table 2 summarizes the author's attempt to investigate the effect of pore-window aperture and size on adsorption and separation properties of alkane molecules by comparing several MOFs with UiO-66.

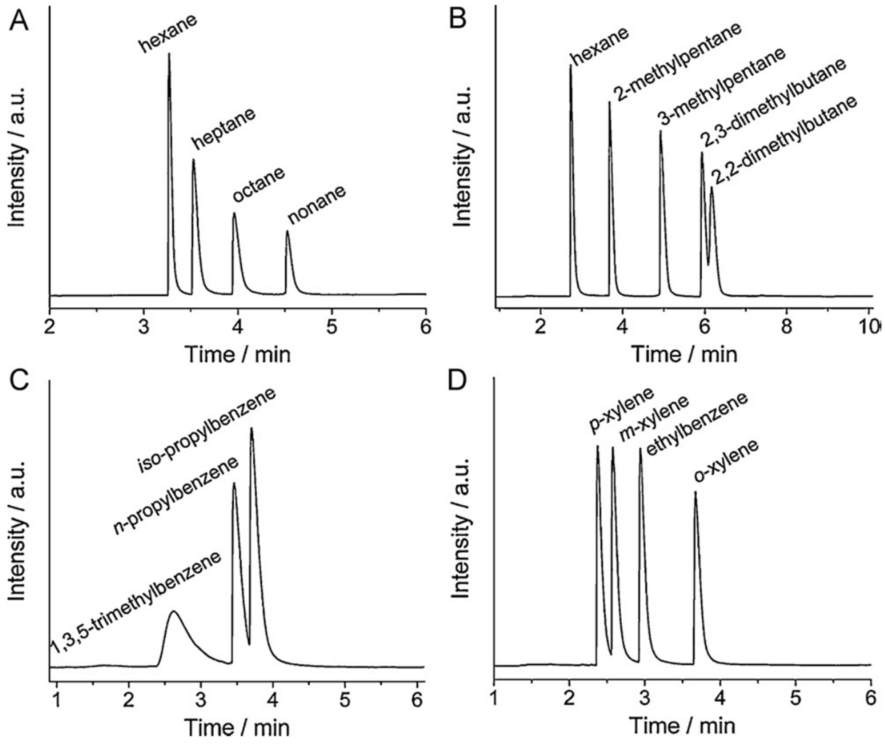



**Figure 16.** Gas chromatograms on the UiO-66 coated capillary column (20 m long × 0.25 mm i.d.) at a $N_2$ flow rate of 1 mL $min^{-1}$ for the separation of: (**A**) hexane, heptane, octane, and nonane using a temperature program of 60 °C for 1 min, and then 40 °C $min^{-1}$ to 250 °C; (**B**) hexane, 2-methylpentane, 3-methylpentane, 2,3-dimethylbutane, and 2,2-dimethylbutane using a temperature program of 100 °C for 1 min, and then 10 °C $min^{-1}$ to 160 °C; (**C**) 1,3,5-trimethylbenzene, n-propylbenzene, and iso-propylbenzene using a temperature program of 140 °C for 1 min, and then 10 °C $min^{-1}$ to 180 °C; (**D**) m-, p-, o-xylene and ethylbenzene using a temperature program of 140 °C for 1 min, and then 10 °C $min^{-1}$ to 180 °C. Reprinted with permission from [73]. Copyright (2012) Elsevier.

**Table 2.** The effect of pore size and pore window size on the adsorption and separation of alkane molecules on several MOFs.

| MOF | Pore Size | Window Size | Alkane Separation |
|---|---|---|---|
| ZIF-7 | 4.31 Å | 2.9 Å | Inaccessible to n-alkanes or iso-alkanes<br>No size or shape selectivity |
| ZIF-8 | 11.6 Å | 3.4 Å | Accessible to n-alkanes<br>Inaccessible to iso-alkanes<br>Size selectivity |
| UIO-66 | 11 Å | 7 Å | Accessible to n-alkanes<br>Accessible small branched alkanes<br>Size and reverse shape selectivity |
| MOF-5 | 18.5 Å | 11.2 Å | Accessible to n-alkanes or iso-alkanes<br>No size or shape selectivity |

Bozbiyik et al. [74] investigated the abovementioned effect of UiO-66 on cycloalkanes. The adsorption and separation of n-hexane and cyclohexane on UiO-66 MOF was studied via IGC. Cyclohexane, which is bulkier and has a higher boiling point than n-hexane, was retained more than n-hexane. The adsorption enthalpy of cyclohexane (−60 kJ $mol^{-1}$) was considerably greater than that of n-hexane (−53 kJ $mol^{-1}$), despite the slightly lower molecular weight. Furthermore, the adsorption entropy of n-hexane was more negative,

demonstrating that the bulkier cyclic molecule loses less freedom in the pores of UiO-66 than the linear n-hexane molecule.

In comparison with linear alkanes, the cyclic alkane has both entropic and enthalpic advantages. The composition of the UiO-66 pore system may explain this. In tetrahedral cages of UiO-66, cyclohexane can maintain a relatively high degree of rotational freedom. The enhanced confinement in these small cages results in a great deal of energetic interaction.

Seeking a deeper understanding of the reverse shape-selectivity performance of UiO-66, the same research group employed IGC at zero coverage for the separation of more than 70 molecules, including alkanes, alkenes, aromatics, and cyclic types on UiO-66 and its derived analogs, such as UiO-66-$NO_2$, UiO-66-Me, and UiO-66-$Me_2$ [75].

High adsorption selectivity indicators were found for cycloalkanes in comparison to n-alkanes, such as the ratio of Henry constants (up to 14). Additional functional groups within the linkers in the framework, such as methyl and nitro groups, markedly affected the adsorption properties, primarily by decreasing the effective pore aperture size. Although improved selectivity for UiO-66-Me was observed, the selectivity decreased when an additional $CH_3$ group was present in UiO-66-$Me_2$. This additional $CH_3$ group enabled confinement factors within the pores, and thus the material's adsorption properties, to be tuned. Selective adsorption was observed as a result of interactions in the smallest octahedral cages. However, intense confinement in the small tetrahedral cage led to stereoselective separation of cis/trans alkenes and disubstituted cycloalkanes. Monte Carlo simulations for pristine UiO-66 MOF and an analysis of the molecular positioning of adsorbates inside the framework supported the experimental results. In addition, the simulations illustrated contributions by entropic factors to the observed selectivity of adsorption.

The effect of chain length on the adsorption of branched and linear alkanes on UiO-66 and its functionalized analogs has also been explored [76]. Characteristic enhancement in Henry constants, adsorption enthalpy, and adsorption entropy occurred at particular carbon chain lengths of n-alkanes for hexane and heptane In case of 2- and 3-methyl alkanes and double branched alkanes, the effect of chain length was even more pronounced. This recognizable change in adsorption took place at a molecular size that matched the pore size of the smallest tetrahedral cages. The resultant selective adsorption emerged from the confinement properties and was a function of the molecule's size and shape.

### 3.6. Other MOFs

Generally, the adsorption properties of MOFs can be modified via chemical functionalization of the MOF pores. Couck et al. [77] examined $SO_2$-DUT-5 and $SO_2$-(Al(OH)(bpdc) MOF (bpdc = 4,4′-biphenyl dicarboxylate)), which is a sulfone-functionalized DUT-5 MOF [126].

The compensation plot (Figure 17) shows the relationship between adsorption entropy and adsorption enthalpy, where the logarithm of pre-exponential factors is presented against the adsorption enthalpies. Generally, a linear connection was witnessed for a group of linear alkanes. The more strongly the probed molecule was adsorbed, the less freedom it had, which was identified as the compensation effect [2,127,128]. This proportional linear connection amongst linear alkanes was perceived for both pristine and $SO_2$-functionalized DUT-5 MOFs. The slopes of the compensation lines, which showed an increase in adsorption entropy with respect to the adsorption enthalpy, were similar for both MOFs, which indicated that they had dissimilar adsorption enthalpies for identical molecules. Thus, the loss of freedom for a given interaction was identical in both MOFs. Thus, the shift in pre-exponential factors between the two MOFs resulted from their different adsorption sites and not from their different entropies of adsorption. Based on that, it was determined that the $SO_2$ functionalization offered better adsorption sites for n-alkane molecules that showed a 4–5 kJ $mol^{-1}$ higher adsorption enthalpy compared to pristine DUT-5.

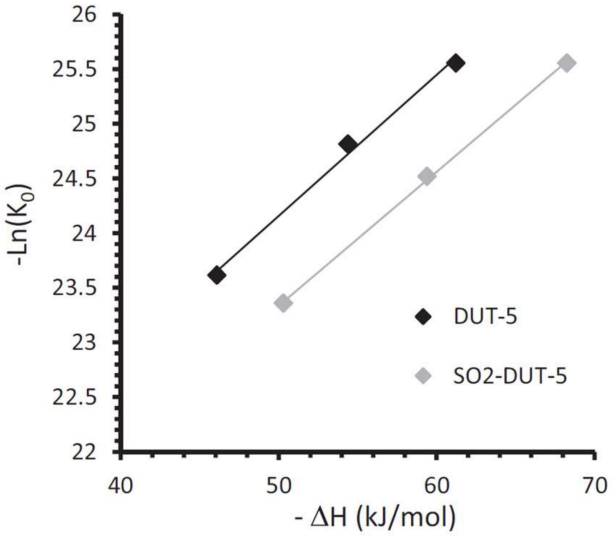



**Figure 17.** Compensation plot of linear alkanes (C5–C7) of $SO_2$-DUT-5 and DUT-5. Reprinted with permission from [77]. Copyright (2015) Elsevier.

$SO_2$-DUT-5 demonstrated shape-selective activity in the adsorption of branched and linear alkanes at low coverage because of the reduction in pore size. In contrast, due its larger pore size, pristine DUT-5 was not shape selective. The ratio of Henry constants of linear and branched alkanes (i.e., separation factors) for all isoalkane/n-alkane pair separations on $SO_2$-DUT-5 were larger than 1.7. DUT-5, in contrast, did not show a marked difference at all for the branched molecules [77].

Alkanes and alkenes adsorbed on $SO_2$-DUT-5 to a similar degree. Although DUT-5 did not have a specific interaction with molecules possessing unsaturated bonds, $SO_2$-DUT-5 demonstrated an improved interaction with aromatic molecules, although this interaction is not very strong and led to only moderate low-pressure separation. Breakthrough studies have shown that at higher pressures and loading, mixtures of aromatics with alkanes or alkenes can be separated, with both pristine and $SO_2$-functionalized DUT-5 MOFs [77]. This distinction is a result of the molecular packing effects rather than specific interactions at a high level of pore filling. Such an effect has already been described several times with other MOFs, for example MIL-47 and MIL-53 [129,130], where separation occurred above a critical level of pore filling, in which the shift occurs from a single alignment of molecules in the one-dimensional pores to a double alignment of molecules.

In conclusion, $SO_2$-DUT-5 showed a slight tendency to adsorb π-bond-containing molecules oversaturated molecules, as indicated by the marginally higher Henry constants for unsaturated compounds. Steric effects and specific adsorption played crucial roles and were correlated to the separation selectivity of alkanes/aromatics, also leading to shape selectivity in isoalkane adsorption. Van der Waals interactions dominated the adsorption properties of DUT-5. Consequently, aromatics, cyclo-alkanes, and alkenes exhibited lower values for both Henry constants and adsorption enthalpies than n-alkanes [77].

Due to its ultramicroporous structure with respect to its molecular dimensions, $Cu(Qc)_2$ [Cu(quinoline-5-carboxyate)$_2$] is a rather attractive MOF [131]. IGC studies were performed on $Cu(Qc)_2$ to determine its surface free energy of adsorption in order to evaluate the affinity between the $O_2/N_2$ mixture [78].

Since $O_2$ and $N_2$ are nonpolar, their surface free energies of adsorption are basically reliant on dispersion forces. The chromatographic peaks illustrated that $N_2$ eluted before $O_2$, which can be accredited to the higher affinity of $Cu(Qc)_2$ towards $O_2$ than $N_2$, or to the high surface free energy or dispersive energy of $O_2$ in comparison to $N_2$ under the same conditions (Figure 18).

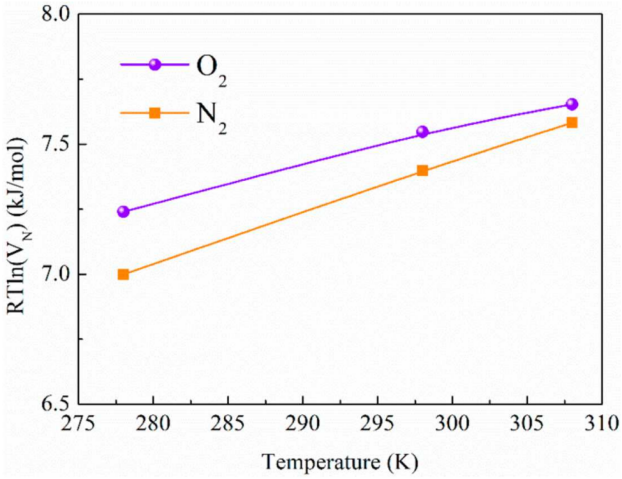



**Figure 18.** Linear dependence of RTln($V_N$) vs. T for the adsorption of $O_2/N_2$. Reprinted with permission from [78] Copyright (2020) Elsevier.

Using a molecular building block (MBB) approach [132,133], a series of RE-**fcu**-MOFs emerged, in which hexanuclear rare earth metal clusters served as twelve interconnected MBBs with face-centered cubic (**fcu**) topology and were connected by fluorinated/nonfluorinated ditopic linkers. The RE-fum-**fcu**-MOF (fum = fumaric acid) constructed from twelve coordinated RE hexanuclear clusters connected by fum showed a high affinity towards hydrocarbon separations [134].

Y-fum-**fcu**-MOF demonstrated the optimum window size for size- and/or shape-selective identification of hydrocarbon isomers with kinetic diameters of approximately 4.7 Å [79]. Assen et al. investigated the adsorption of $C_4$ alkenes with kinetic diameters between linear and branched $C_4$ alkanes. Different techniques were used, including IGC, to determine adsorption at infinite dilution and confirm the capacity of Y-fum-**fcu**-MOF for these separations. The retention time for butene isomer GC separation depended on two factors: the accessibility of adsorbates to the pores and the enthalpy of adsorption after the molecules accessed the pores. In spite of the comparable $\Delta H_{ads}$ for cis and trans-2-butene, a result of their similar chemical natures, the molecule shape and size were the key factors in determining the adsorption selectivity [79].

## 4. Future Outlook

There are many applications of MOFs that depend on their adsorption properties. Hence, we have reviewed the utilization of IGC as a tool to investigate the physicochemical features of MOFs. IGC has helped to evaluate and predict the ability of MOF surfaces to contribute in both dispersive and specific interactions. Unlike an analytical GC technique, in IGC the roles of the mobile and stationary phases are reversed. This means that the material under study becomes the stationary phase and the injected well-known molecules within the mobile phase are probes, which are used to investigate the physicochemical properties of the stationary phase.

An excellent agreement has been revealed between the IGC-measured enthalpies of adsorption, and those estimated using other surface energy analysis techniques, such as calorimetric, volumetric, or gravimetric measurements, and even molecular modeling measurements. Moreover, IGC showed shorter experimental times compared to other techniques without almost any specific preparation of samples for crystalline or amorphous materials. The probability of observing the differences associated with surface group orientations is one of the benefits of using IGC in researching acid- and base-specific properties.

The total solid surface energy is represented by the summation of the dispersive and specific properties. From the thermodynamic properties of a material, its adsorption behavior can be interpreted and predicted. For instance, a plot of the Henry constants logarithm

versus the vapor pressure logarithm could be used to investigate whether the material's ability to discriminate between branched and linear alkanes is related to a size-exclusion property. The difference between enthalpy of adsorption and its vaporization analogue is how they demonstrate the strength of adsorption toward the tested probe. Imperfections due to the degradation of MOFs could also be detected by a large value for the entropy of adsorption. Moreover, the activity of the MOF material under examination could be measured and compared with classical microporous materials via the dispersive component of the surface energy as a function of London interactions and surface heterogeneity.

Some considerations should be accounted for while using the IGC technique. A minimal amount of testing probes should be used in order to maintain a monolayer surface coverage. The peak symmetry is should also be carefully controlled, as the precise retention time is a basic source of the subsequent data. Optimum flowrate should be estimated via the Van Deemter curve, as a higher flowrate prevents the system's equilibrium, and a lower flowrate means broader peaks and longer experimental times. The surface area of the examined material must be measured accurately, as it becomes one of the basic properties utilized in further measurements. The molecular area of the polar probes most used in IGC is another issue to be considered as the literature shows a different value for those probes; however, a recent study [135] addressed that problem.

Past research on a variety of materials has proved that the IGC technique can be fruitfully implemented to characterize the surface and bulk properties of solids based on their diverse morphologies and shapes. However, IGC as a tool for MOF characterization is still in its infancy and much of this area remains to be discovered. IGC is adaptable, accurate, and simple, attributes that can cement its position as an essential characterization technique in MOF research. While some MOFs have been investigated using IGC and revealed great potential, many others are still waiting. In addition, many more parameters of MOFs may be evaluated, such as shape, morphology, topology index [136], and surface area measurements [137].

**Author Contributions:** Conceptualization, K.Y.; methodology, K.Y. and O.S.; software, K.Y. and O.S.; validation, K.Y., O.S., Z.A. and M.E.; formal analysis, K.Y. and O.S.; investigation, O.S.; resources, K.Y. and O.S.; data curation, K.Y.; writing—original draft preparation, K.Y. and O.S.; writing—review and editing, K.Y. and O.S.; visualization, O.S.; supervision, Z.A. and M.E.; project administration, Z.A. and M.E.; funding acquisition, K.Y. All authors have read and agreed to the published version of the manuscript.

**Funding:** This project was funded by the National Plan for Science, Technology, and Innovation (MAARIFAH), King Abdul Aziz City for Science and Technology, Kingdom of Saudi Arabia, grant number 14-ADV2447-02.

**Acknowledgments:** The authors acknowledge the National Plan for Science, Technology, and Innovation (MAARIFAH), King Abdulaziz City for Science and Technology, Kingdom of Saudi Arabia for its grant with award number 14-ADV2447-02.

**Conflicts of Interest:** The authors declare no conflict of interest.

## References

1. Barrer, R.M.; Sutherland, J.W. Inclusion complexes of faujasite with paraffins and permanent gases. *Proc. R. Soc. Lond. Ser. A Math. Phys. Sci.* **1956**, *237*, 439–463. [CrossRef]
2. Eder, F.; Lercher, J.A. On the role of the pore size and tortuosity for sorption of alkanes in molecular sieves. *J. Phys. Chem. B* **1997**, *101*, 1273–1278. [CrossRef]
3. Hufton, J.R.; Danner, R.P. Chromatographic study of alkanes in silicalite: Equilibrium properties. *AIChE J.* **1993**, *39*, 954–961. [CrossRef]
4. Jänchen, J.; Stach, H. Dependence of the adsorption equilibrium of n-decane on the Si Al-ratio of faujasite-zeolites. *Zeolites* **1985**, *5*, 57–59. [CrossRef]
5. Richards, R.E.; Rees, L.V.C. Sorption and Packing of n-Alkane Molecules in ZSM-5+. *Langmuir* **1987**, *3*, 335–340. [CrossRef]
6. Stach, H.; Lohse, U.; Thamm, H.; Schirmer, W. Adsorption equilibria of hydrocarbons on highly dealuminated zeolites. *Zeolites* **1986**, *6*, 74–90. [CrossRef]

7. Sun, M.S.; Talu, O.; Shah, D.B. Adsorption equilibria of C5-C10 normal alkanes in silicalite crystals. *J. Phys. Chem.* **1996**, *100*, 17276–17280. [CrossRef]
8. Thamm, H.; Stach, H.; Fiebig, W. Calorimetric study of the absorption of n-butane and but-l-ene on a highly dealuminated Y-type zeolite and on silicalite. *Zeolites* **1983**, *3*, 95–97. [CrossRef]
9. Eder, F.; Lercher, J.A. Alkane sorption on siliceous and aluminophosphate molecular sieves. A comparative study. *J. Phys. Chem.* **1996**, *100*, 16460–16462. [CrossRef]
10. Liu, B.; Smit, B.; Rey, F.; Valencia, A.S.; Calero, S. A new united atom force field for adsorption of alkenes in zeolites. *J. Phys. Chem. C* **2008**, *112*, 2492–2498. [CrossRef]
11. De Meyer, K.M.A.; Chempath, S.; Denayer, J.F.M.; Martens, J.A.; Snurr, A.R.Q.; Baron, G.V. Packing effects in the liquid-phase adsorption of C5–C22 n-alkanes on ZSM-5. *J. Phys. Chem. B* **2003**, *107*, 10760–10766. [CrossRef]
12. Daems, I.; Baron, G.V.; Punnathanam, S.; Snurr, A.R.Q.; Denayer, J.F.M. Molecular cage nestling in the liquid-phase adsorption of n-Alkanes in 5A zeolite. *J. Phys. Chem. C* **2007**, *111*, 2191–2197. [CrossRef]
13. Stapley, J.; Buckton, G.; Merrifield, D. Investigation to find a suitable reference material for use as an inverse gas chromatography system suitability test. *Int. J. Pharm.* **2006**, *318*, 22–27. [CrossRef]
14. Díaz, E.; Ordóñez, S.; Auroux, A. Comparative study on the gas-phase adsorption of hexane over zeolites by calorimetry and inverse gas chromatography. *J. Chromatogr. A* **2005**, *1095*, 131–137. [CrossRef] [PubMed]
15. Thielmann, F. Introduction into the characterisation of porous materials by inverse gas chromatography. *J. Chromatogr. A* **2004**, *1037*, 115–123. [CrossRef] [PubMed]
16. Voelkel, A.; Strzemiecka, B.; Adamska, K.; Milczewska, K. Inverse gas chromatography as a source of physiochemical data. *J. Chromatogr. A* **2009**, *1216*, 1551–1566. [CrossRef] [PubMed]
17. Vista, M. LAYLIN K. JAMES (ed.), Nobel Laureates in Chemistry, 1901–1992. Washington, American Chemical Society and the Chemical Heritage Foundation, 1993, XVIII + 798 pp. (History of Modern Chemical Sciences). *Nuncius* **2012**, *9*, 940–942. [CrossRef]
18. Butler, D.; Williams, D.R. Particulate characterization: Inverse gas chromatography. In *Encyclopedia of Separation Science*; Elsevier: Amsterdam, The Netherlands, 2000; pp. 3609–3614. [CrossRef]
19. Yashin, Y.I.; Andrej, V. Kiselev's contributions to the science of adsorption, molecular interaction and chromatography. *Pure Appl. Chem.* **1989**, *61*, 1829–1834. [CrossRef]
20. Smidsrϕd, O.; Guillet, J.E. Study of polymer–solute interactions by gas chromatography. *Macromolecules* **1969**, *2*, 272–277. [CrossRef]
21. Novák, J. Physicochemical measurement by gas chromatography. *J. Chromatogr. A* **1980**, *187*, 283–284. [CrossRef]
22. Mohammadi-Jam, S.; Waters, K.E. Inverse gas chromatography applications: A review. *Adv. Colloid Interface Sci.* **2014**, *212*, 21–44. [CrossRef] [PubMed]
23. Nelsen, F.M.; Eggertsen, F.T. Determination of surface area: Adsorption measurements by a continuous flow method. *Anal. Chem.* **1958**, *30*, 1387–1390. [CrossRef]
24. Münch, A.S.; Mertens, F.O.R.L. The Lewis acidic and basic character of the internal HKUST-1 surface determined by inverse gas chromatography. *CrystEngComm* **2015**, *17*, 438–447. [CrossRef]
25. Luner, P.E.; Zhang, Y.; Abramov, Y.A.; Carvajal, M.T. Evaluation of milling method on the surface energetics of molecular crystals using inverse gas chromatography. *Cryst. Growth Des.* **2012**, *12*, 5271–5282. [CrossRef]
26. Menzel, R.; Bismarck, A.; Shaffer, M.S.P. Deconvolution of the structural and chemical surface properties of carbon nanotubes by inverse gas chromatography. *Carbon N. Y.* **2012**, *50*, 3416–3421. [CrossRef]
27. Voelkel, A. Inverse gas chromatography: Characterization of polymers, fibers, modified silicas, and surfactants. *Crit. Rev. Anal. Chem.* **1991**, *22*, 411–439. [CrossRef]
28. Wang, W.; Kale, V.S.; Cao, Z.; Kandambeth, S.; Zhang, W.; Ming, J.; Parvatkar, P.T.; Abou-Hamad, E.; Shekhah, O.; Cavallo, L.; et al. Phenanthroline covalent organic framework electrodes for high-performance zinc-ion supercapattery. *ACS Energy Lett.* **2020**, *5*, 2256–2264. [CrossRef]
29. Yuvaraja, S.; Surya, S.G.; Chernikova, V.; Vijjapu, M.T.; Shekhah, O.; Bhatt, P.M.; Chandra, S.; Eddaoudi, M.; Salama, K.N. Realization of an ultrasensitive and highly selective OFET $NO_2$ sensor: The synergistic combination of PDVT-10 polymer and porphyrin-MOF. *ACS Appl. Mater. Interfaces* **2020**, *12*, 18748–18760. [CrossRef]
30. Chernikova, V.; Shekhah, O.; Belmabkhout, Y.; Eddaoudi, M. Nanoporous fluorinated metal-organic framework-based membranes for $CO_2$ capture. *ACS Appl. Nano Mater.* **2020**, *3*, 6432–6439. [CrossRef]
31. Jiang, H.; Alezi, D.; Eddaoudi, M. A reticular chemistry guide for the design of periodic solids. *Nat. Rev. Mater.* **2021**, *6*, 466–487. [CrossRef]
32. Chen, Z.; Jiang, H.; Li, M.; O'Keeffe, M.; Eddaoudi, M. Reticular chemistry 3.2: Typical minimal edge-transitive derived and related nets for the design and synthesis of metal-organic frameworks. *Chem. Rev.* **2020**, *120*, 8039–8065. [CrossRef] [PubMed]
33. Li, J.; Bhatt, P.M.; Li, J.; Eddaoudi, M.; Liu, Y. Recent progress on microfine design of metal–organic frameworks: Structure regulation and gas sorption and separation. *Adv. Mater.* **2020**, *32*. [CrossRef] [PubMed]
34. Nam, D.H.; Shekhah, O.; Lee, G.; Mallick, A.; Jiang, H.; Li, F.; Chen, B.; Wicks, J.; Eddaoudi, M.; Sargent, E.H. Intermediate binding control using metal-organic frameworks enhances electrochemical $CO_2$ reduction. *J. Am. Chem. Soc.* **2020**, *142*, 21513–21521. [CrossRef] [PubMed]

35. Jia, Z.; Wu, G. Metal-organic frameworks based mixed matrix membranes for pervaporation. *Microporous Mesoporous Mater.* **2016**, *235*, 151–159. [CrossRef]
36. Cui, W.G.; Hu, T.L.; Bu, X.H. Metal–organic framework materials for the separation and purification of light hydrocarbons. *Adv. Mater.* **2020**, *32*, 1806445. [CrossRef] [PubMed]
37. Tang, W.; Xu, J.; Gu, Z. Metal–organic-framework-based gas chromatographic separation. *Chem. Asian J.* **2019**, *14*, 3462–3473. [CrossRef]
38. Rieger, M.; Wittek, M.; Scherer, P.; Löbbecke, S.; Müller-Buschbaum, K. Preconcentration of nitroalkanes with archetype metal–organic frameworks (MOFs) as concept for a sensitive sensing of explosives in the gas phase. *Adv. Funct. Mater.* **2018**, *28*, 1–11. [CrossRef]
39. Thielmann, F.; Butler, D.A.; Williams, D.R.; Baumgarten, E. Characterisation of microporous materials by dynamic sorption methods. *Stud. Surf. Sci. Catal.* **2000**, *129*, 633–638. [CrossRef]
40. Mukhopadhyay, P.; Schreiber, H.P. Aspects of acid-base interactions and use of inverse gas chromatography. *Colloids Surf. A Physicochem. Eng. Asp.* **1995**, *100*, 47–71. [CrossRef]
41. Tijburg, I.; Jagiello, J.; Vidal, A.; Papirer, E. Inverse gas chromatographic studies on silica: Infinite dilution and finite concentration measurements. *Langmuir* **1991**, *7*, 2243–2247. [CrossRef]
42. Balard, H. Estimation of the surface energetic heterogeneity of a solid by inverse gas chromatography. *Langmuir* **1997**, *13*, 1260–1269. [CrossRef]
43. Thielmann, F.; Butler, D.A.; Williams, D.R. Characterization of porous materials by finite concentration inverse gas chromatography. *Colloids Surf. A Physicochem. Eng. Asp.* **2001**, *187–188*, 267–272. [CrossRef]
44. Lavielle, L.; Schultz, J. Surface properties of carbon fibers determined by inverse gas chromatography: Role of pretreatment. *Langmuir* **1991**, *7*, 978–981. [CrossRef]
45. James, A.T.; Martin, A.J. Gas-liquid partition chromatography; the separation and micro-estimation of volatile fatty acids from formic acid to dodecanoic acid. *Biochem. J.* **1952**, *50*, 679–690. [CrossRef]
46. Mäihäniemi-Ylä, P.P.; Williams, D.R. A comparison of frontal and nonfrontal methods for determining solid-liquid adsorption isotherms using inverse liquid chromatography. *Langmuir* **2007**, *23*, 4095–4101. [CrossRef] [PubMed]
47. Littlewood, A.B.; Phillips, C.S.G.; Price, D.T. The chromatography of gases and vapours. Part V. Partition analyses with columns of silicone 702 and of tritolyl phosphate. *J. Chem. Soc.* **1955**, 1480–1489. [CrossRef]
48. Katsanos, N.A.; Thede, R.; Roubani-Kalantzopoulou, F. Diffusion, adsorption and catalytic studies by gas chromatography. *J. Chromatogr. A* **1998**, *795*, 133–184. [CrossRef]
49. Finsy, V.; de Bruyne, S.; Alaerts, L.; de Vos, D.; Jacobs, P.A.; Baron, G.V.; Denayer, J.F.M. Shape selective adsorption of linear and branched alkanes in the $Cu_3$(BTC)2 metal-organic framework. In *Studies in Surface Science and Catalysis*; Elsevier B.V.: Amsterdam, The Nehterlands, 2007. [CrossRef]
50. Fowkes, F.M. Attractive forces at interfaces. *Ind. Eng. Chem.* **1964**, *56*, 40–52. [CrossRef]
51. Dorris, G.M.; Gray, D.G. Adsorption of n-alkanes at zero surface coverage on cellulose paper and wood fibers. *J. Colloid Interface Sci.* **1980**, *77*, 353–362. [CrossRef]
52. Schultz, J.; Martin, C. The role of the interface in carbon fibre-epoxy compositest. *J. Adhes.* **1987**, *23*, 45–60. [CrossRef]
53. Pefferkorn, E. *Interfacial Phenomena in Chromatography*; Routledge: London, UK, 1999. [CrossRef]
54. Brookman, D.J.; Sawyer, D.T. Specific interactions affecting gas chromatographic retention for modified alumina columns. *Anal. Chem.* **1968**, *40*, 106–110. [CrossRef]
55. Riddle, F.L.; Fowkes, F.M. Spectral shifts in acid-base chemistry. 1. Van der Waals Contributions to Acceptor Numbers. *J. Am. Chem. Soc.* **1990**, *112*, 3259–3264. [CrossRef]
56. Schuster, P. The donor-acceptor approach to molecular interactions. *Fluid Phase Equilib.* **1979**, *3*, 251–252. [CrossRef]
57. Autie-Castro, G.; Autie, M.A.; Rodríguez-Castellón, E.; Aguirre, C.; Reguera, E. Cu-BTC and Fe-BTC metal-organic frameworks: Role of the materials structural features on their performance for volatile hydrocarbons separation. *Colloids Surf. A Physicochem. Eng. Asp.* **2015**, *481*, 351–357. [CrossRef]
58. Gutiérrez, I.; Díaz, E.; Vega, A.; Ordóñez, S.; Guerrero-Ruiz, A.; Castillejos-López, E.; Rodríguez-Ramos, I. Hydrocarbons adsorption on metal trimesate MOFs: Inverse gas chromatography and immersion calorimetry studies. *Thermochim. Acta* **2015**, *602*, 36–42. [CrossRef]
59. Autié-Castro, G.; Reguera, E.; Cavalcante, C.L.; Araujo, A.S.; Rodríguez-Castellón, E. Surface acid-base properties of Cu-BTC and Fe-BTC MOFs. An inverse gas chromatography and n-butylamine thermo desorption study. *Inorg. Chim. Acta* **2020**, *507*, 119590. [CrossRef]
60. Finsy, V.; Calero, S.; García-Pérez, E.; Merkling, P.J.; Vedts, G.; de Vos, D.E.; Baron, G.V.; Denayer, J.F.M. Low-coverage adsorption properties of the metal-organic framework MIL-47 studied by pulse chromatography and Monte Carlo simulations. *Phys. Chem. Chem. Phys.* **2009**, *11*, 3515–3521. [CrossRef] [PubMed]
61. Duerinck, T.; Couck, S.; Vermoortele, F.; de Vos, D.E.; Baron, G.V.; Denayer, J.F.M. Pulse gas chromatographic study of adsorption of substituted aromatics and heterocyclic molecules on MIL-47 at zero coverage. *Langmuir* **2012**, *28*, 13883–13891. [CrossRef]
62. Couck, S.; Rémy, T.; Baron, G.V.; Gascon, J.; Kapteijn, F.; Denayer, J.F.M. A pulse chromatographic study of the adsorption properties of the amino-MIL-53 (Al) metal-organic framework. *Phys. Chem. Chem. Phys.* **2010**, *12*, 9413–9418. [CrossRef]

63. Sun, T.; Ren, X.; Hu, J.; Wang, S. Expanding pore size of Al-BDC metal-organic frameworks as a way to achieve high adsorption selectivity for $CO_2/CH_4$ separation. *J. Phys. Chem. C.* **2014**, *118*, 15630–15639. [CrossRef]
64. Sun, T.; Hu, J.; Ren, X.; Wang, S. Experimental evaluation of the adsorption, diffusion, and separation of $CH_4/N_2$ and $CH_4/CO_2$ mixtures on Al-BDC MOF. *Sep. Sci. Technol.* **2015**, *50*, 874–885. [CrossRef]
65. Zhao, Z.; Li, X.; Li, Z. Adsorption equilibrium and kinetics of p-xylene on chromium-based metal organic framework MIL-101. *Chem. Eng. J.* **2011**, *173*, 150–157. [CrossRef]
66. Gu, Z.Y.; Jiang, D.Q.; Wang, H.F.; Cui, X.Y.; Yan, X.P. Adsorption and separation of xylene isomers and ethylbenzene on two Zn-terephthalate metal-organic frameworks. *J. Phys. Chem. C.* **2010**, *114*, 311–316. [CrossRef]
67. Luebbers, M.T.; Wu, T.; Shen, L.; Masel, R.I. Trends in the adsorption of volatile organic compounds in a large-pore metal-organic framework, IRMOF-1. *Langmuir* **2010**, *26*, 11319–11329. [CrossRef] [PubMed]
68. Gutiérrez, I.; Díaz, E.; Vega, A.; Ordóñez, S. Consequences of cavity size and chemical environment on the adsorption properties of isoreticular metal-organic frameworks: An inverse gas chromatography study. *J. Chromatogr. A* **2013**, *1274*, 173–180. [CrossRef]
69. Luebbers, M.T.; Wu, T.; Shen, L.; Masel, R.I. Effects of molecular sieving and electrostatic enhancement in the adsorption of organic compounds on the zeolitic imidazolate framework ZIF-8. *Langmuir* **2010**, *26*, 15625–15633. [CrossRef]
70. Virdis, T.; Danilov, V.; Baron, G.V.; Denayer, J.F.M. Nonideality in the adsorption of ethanol/ethyl acetate/water mixtures on ZIF-8 metal organic framework. *Ind. Eng. Chem. Res.* **2018**, *57*, 7040–7047. [CrossRef]
71. Yusuf, K.; Badjah-Hadj-Ahmed, A.Y.; Aqel, A.; Aouak, T.; Othman, Z.A.A.L. Zeolitic imidazolate framework-methacrylate composite monolith characterization by inverse gas chromatography. *J. Chromatogr. A* **2016**, *1443*, 233–240. [CrossRef] [PubMed]
72. Van der Perre, S.; Bozbiyik, B.; Lannoeye, J.; de Vos, D.E.; Baron, G.V.; Denayer, J.F.M. Experimental study of adsorptive interactions of polar and nonpolar adsorbates in the Zeolitic Imidazolate Framework ZIF-68 via pulse gas chromatography. *J. Phys. Chem. C* **2015**, *119*, 1832–1839. [CrossRef]
73. Chang, N.; Yan, X.P. Exploring reverse shape selectivity and molecular sieving effect of metal-organic framework UIO-66 coated capillary column for gas chromatographic separation. *J. Chromatogr. A* **2012**, *1257*, 116–124. [CrossRef]
74. Bozbiyik, B.; Duerinck, T.; Lannoeye, J.; de Vos, D.E.; Baron, G.V.; Denayer, J.F.M. Adsorption and separation of n-hexane and cyclohexane on the UiO-66 metal-organic framework. *Microporous Mesoporous Mater.* **2014**, *183*, 143–149. [CrossRef]
75. Duerinck, T.; Bueno-Perez, R.; Vermoortele, F.; de Vos, D.E.; Calero, S.; Baron, G.V.; Denayer, J.F.M. Understanding hydrocarbon adsorption in the uio-66 metal-organic framework: Separation of (un)saturated linear, branched, cyclic adsorbates, including stereoisomers. *J. Phys. Chem. C* **2013**, *117*, 12567–12578. [CrossRef]
76. Duerinck, T.; Denayer, J.F.M. Unusual chain length dependent adsorption of linear and branched alkanes on UiO-66. *Adsorption* **2014**, *20*, 251–259. [CrossRef]
77. Couck, S.; Liu, Y.Y.; Leus, K.; Baron, G.V.; van der Voort, P.; Denayer, J.F.M. Gas phase adsorption of alkanes, alkenes and aromatics on the sulfone-DUT-5 metal organic framework. *Microporous Mesoporous Mater.* **2015**, *206*, 217–225. [CrossRef]
78. Tang, Y.; Wang, X.; Wen, Y.; Zhou, X.; Li, Z. Oxygen-selective adsorption property of ultramicroporous MOF Cu(Qc)2 for air separation. *Ind. Eng. Chem. Res.* **2020**, *59*, 6219–6225. [CrossRef]
79. Assen, A.H.; Virdis, T.; de Moor, W.; Moussa, A.; Eddaoudi, M.; Baron, G.; Denayer, J.F.M.; Belmabkhout, Y. Kinetic separation of C4 olefins using Y-fum-fcu-MOF with ultra-fine-tuned aperture size. *Chem. Eng. J.* **2021**, *413*, 127388. [CrossRef]
80. Chui, S.S.Y.; Lo, S.M.F.; Charmant, J.P.H.; Orpen, A.G.; Williams, I.D. A chemically functionalizable nanoporous material $[Cu_3(TMA)_2\ (H_2O)_3]$(n). *Science* **1999**, *283*, 1148–1150. [CrossRef]
81. Peralta, D.; Chaplais, G.; Simon-Masseron, A.; Barthelet, K.; Chizallet, C.; Quoineaud, A.A.; Pirngruber, G.D. Comparison of the behavior of metal-organic frameworks and zeolites for hydrocarbon separations. *J. Am. Chem. Soc.* **2012**, *134*, 8115–8126. [CrossRef]
82. Wu, D.; Guo, X.; Sun, H.; Navrotsky, A. Interplay of confinement and surface energetics in the interaction of water with a metal-organic framework. *J. Phys. Chem. C* **2016**, *120*, 7562–7567. [CrossRef]
83. Dathe, H.; Peringer, E.; Roberts, V.; Jentys, A.; Lercher, J.A. Metal organic frameworks based on Cu2+ and benzene-1,3,5-tricarboxylate as host for SO2 trapping agents. *C. R. Chim.* **2005**, *8*, 753–763. [CrossRef]
84. Krawiec, P.; Kramer, M.; Sabo, M.; Kunschke, R.; Fröde, H.; Kaskel, S. Improved hydrogen storage in the Metal-Organic Framework Cu 3(BTC)2. *Adv. Eng. Mater.* **2006**, *8*, 293–296. [CrossRef]
85. Prestipino, C.; Regli, L.; Vitillo, J.G.; Bonino, F.; Damin, A.; Lamberti, C.; Zecchina, A.; Solari, P.L.; Kongshaug, K.O.; Bordiga, S. Local structure of framework Cu(II) in HKUST-1 metallorganic framework: Spectroscopic characterization upon activation and interaction with adsorbates. *Chem. Mater.* **2006**, *18*, 1337–1346. [CrossRef]
86. Zhu, B.J.; Yu, X.Y.; Jia, Y.; Peng, F.M.; Sun, B.; Zhang, M.Y.; Luo, T.; Liu, J.H.; Huang, X.J. Iron and 1,3,5-benzenetricarboxylic metal-organic coordination polymers prepared by solvothermal method and their application in efficient as(V) removal from aqueous solutions. *J. Phys. Chem. C* **2012**, *116*, 8601–8607. [CrossRef]
87. Eddaoudi, M.; Kim, J.; Vodak, D.; Sudik, A.; Wachter, J.; O'Keeffe, M.; Yaghi, O.M. Geometric requirements and examples of important structures in the assembly of square building blocks. *Proc. Natl. Acad. Sci. USA* **2002**, *99*, 4900–4904. [CrossRef] [PubMed]
88. Park, K.S.; Ni, Z.; Côté, A.P.; Choi, J.Y.; Huang, R.; Uribe-Romo, F.J.; Chae, H.K.; O'Keeffe, M.; Yaghi, O.M. Exceptional chemical and thermal stability of zeolitic imidazolate frameworks. *Proc. Natl. Acad. Sci. USA* **2006**, *103*, 10186–10191. [CrossRef] [PubMed]
89. Webster, C.E.; Drago, R.S.; Zerner, M.C. Molecular dimensions for adsorptives. *J. Am. Chem. Soc.* **1998**, *120*, 5509–5516. [CrossRef]

90. Barthelet, K.; Marrot, J.; Riou, D.; Férey, G. A breathing hybrid organic-inorganic solid with very large pores and high magnetic characteristics. *Angew. Chem. Int. Ed.* **2002**, *41*, 281–284. [CrossRef]
91. Serre, C.; Millange, F.; Thouvenot, C.; Noguès, M.; Marsolier, G.; Louër, D.; Férey, G. Very large breathing effect in the first nanoporous chromium(III)-based solids: MIL-53 or CrIII(OH)·{$O_2$C-$C_6H_4$- $CO_2$}·{$HO_2$C-$C_6H_4$-$CO_2$H}x·$H_2$Oy. *J. Am. Chem. Soc.* **2002**, *124*, 13519–13526. [CrossRef] [PubMed]
92. Kitagawa, S.; Kitaura, R.; Noro, S.I. Functional porous coordination polymers. *Angew. Chem. Int. Ed.* **2004**, *43*, 2334–2375. [CrossRef]
93. Serre, C.; Bourrelly, S.; Vimont, A.; Ramsahye, N.A.; Maurin, G.; Llewellyn, P.L.; Daturi, M.; Filinchuk, Y.; Leynaud, O.; Barnes, P.; et al. An explanation for the very large breathing effect of a metal-organic framework during $CO_2$ adsorption. *Adv. Mater.* **2007**, *19*, 2246–2251. [CrossRef]
94. Bourrelly, S.; Llewellyn, P.L.; Serre, C.; Millange, F.; Loiseau, T.; Férey, G. Different adsorption behaviors of methane and carbon dioxide in the isotypic nanoporous metal terephthalates MIL-53 and MIL-47. *J. Am. Chem. Soc.* **2005**, *127*, 13519–13521. [CrossRef] [PubMed]
95. Couck, S.; Denayer, J.F.M.; Baron, G.V.; Rémy, T.; Gascon, J.; Kapteijn, F. An amine-functionalized MIL-53 metal-organic framework with large separation power for $CO_2$ and $CH_4$. *J. Am. Chem. Soc.* **2009**, *131*, 6326–6327. [CrossRef] [PubMed]
96. Devic, T.; Horcajada, P.; Serre, C.; Salles, F.; Maurin, G.; Moulin, B.; Heurtaux, D.; Clet, G.; Vimont, A.; Grenéche, J.M.; et al. Functionalization in flexible porous solids: Effects on the pore opening and the host-guest interactions. *J. Am. Chem. Soc.* **2010**, *132*, 1127–1136. [CrossRef]
97. Ahnfeldt, T.; Gunzelmann, D.; Loiseau, T.; Hirsemann, D.; Senker, J.; Férey, G.; Stock, N. Synthesis and modification of a functionalized 3D open-framework structure with MIL-53 topology. *Inorg. Chem.* **2009**, *48*, 3057–3064. [CrossRef] [PubMed]
98. Millange, F.; Serre, C.; Férey, G. Synthesis, structure determination and properties of MIL-53as and MIL-53ht: The first CrIII hybrid inorganic-organic microporous solids: CrIII(OH)·($O_2$C-$C_6H_4$-$CO_2$)·($HO_2$C-$C_6H_4$-$CO_2$H)x. *Chem. Commun.* **2002**, *2*, 822–823. [CrossRef]
99. Alaerts, L.; Kirschhock, C.E.A.; Maes, M.; van der Veen, M.A.; Finsy, V.; Depla, A.; Martens, J.A.; Baron, G.V.; Jacobs, P.A.; Denayer, J.F.M.; et al. Selective adsorption and separation of xylene isomers and ethylbenzene with the microporous vanadium(IV) terephthalate MIL-47. *Angew. Chem. Int. Ed.* **2007**, *46*, 4293–4297. [CrossRef] [PubMed]
100. Llewellyn, P.L.; Bourrelly, S.; Serre, C.; Vimont, A.; Daturi, M.; Hamon, L.; de Weireld, G.; Chang, J.S.; Hong, D.Y.; Hwang, Y.K.; et al. High uptakes of $CO_2$ and $CH_4$ in mesoporous metal-organic frameworks MIL-100 and MIL-101. *Langmuir* **2008**, *24*, 7245–7250. [CrossRef] [PubMed]
101. Eddaoudi, M.; Kim, J.; Rosi, N.; Vodak, D.; Wachter, J.; O'Keeffe, M.; Yaghi, O.M. Systematic design of pore size and functionality in isoreticular MOFs and their application in methane storage. *Science* **2002**, *295*, 469–472. [CrossRef]
102. Li, H.; Eddaoudi, M.; O'Keeffe, M.; Yaghi, O.M. Design and synthesis of an exceptionally stable and highly porous metal- organic framework. *Nature* **1999**, *402*, 276–279. [CrossRef]
103. Edgar, M.; Mitchell, R.; Slawin, A.M.Z.; Lightfoot, P.; Wright, P.A. Solid-State transformations of zinc 1,4-benzenedicarboxylates mediated by hydrogen-bond-forming molecules. *Chem. Eur. J.* **2001**, *7*, 5168. [CrossRef]
104. Biemmi, E.; Christian, S.; Stock, N.; Bein, T. High-throughput screening of synthesis parameters in the formation of the metal-organic frameworks MOF-5 and HKUST-1. *Microporous Mesoporous Mater.* **2009**, *117*, 111–117. [CrossRef]
105. Choi, J.S.; Son, W.J.; Kim, J.; Ahn, W.S. Metal-organic framework MOF-5 prepared by microwave heating: Factors to be considered. *Microporous Mesoporous Mater.* **2008**, *116*, 727–731. [CrossRef]
106. Hafizovic, J.; Bjørgen, M.; Olsbye, U.; Dietzel, P.D.C.; Bordiga, S.; Prestipino, C.; Lamberti, C.; Lillerud, K.P. The inconsistency in adsorption properties and powder XRD data of MOF-5 is rationalized by framework interpenetration and the presence of organic and inorganic species in the nanocavities. *J. Am. Chem. Soc.* **2007**, *129*, 3612–3620. [CrossRef] [PubMed]
107. Hausdorf, S.; Wagler, J.; Mossig, R.; Mertens, F.O.R.L. Proton and water activity-controlled structure formation in zinc carboxylate-based metal organic frameworks. *J. Phys. Chem. A* **2008**, *112*, 7567–7576. [CrossRef]
108. Jiang, J.; Sandler, S.I. Monte Carlo simulation for the adsorption and separation of linear and branched alkanes in IRMQF-1. *Langmuir* **2006**, *22*, 5702–5707. [CrossRef] [PubMed]
109. Almazán-Almazán, M.C.; Pérez-Mendoza, M.; Domingo-García, M.; Fernández-Morales, I.; del Rey-Bueno, F.; García-Rodríguez, A.; López-Garzón, F.J. The role of the porosity and oxygen groups on the adsorption of n-alkanes, benzene, trichloroethylene and 1,2-dichloroethane on active carbons at zero surface coverage. *Carbon N. Y.* **2007**, *45*, 1777–1785. [CrossRef]
110. Herry, C.; Baudu, M.; Raveau, D. Estimation of the influence of structural elements of activated carbons on the energetic components of adsorption. *Carbon N. Y.* **2001**, *39*, 1879–1889. [CrossRef]
111. Mäihäniemi-Ylä, P.P.; Heng, J.Y.Y.; Thielmann, F.; Williams, D.R. Inverse gas chromatographic method for measuring the dispersive surface energy distribution for particulates. *Langmuir* **2008**, *24*, 9551–9557. [CrossRef]
112. Pearce, H.A. Zeolite molecular sieves—Structure, chemistry and use. *J. Chromatogr. A* **1975**, *106*, 499. [CrossRef]
113. Pérez-Pellitero, J.; Amrouche, H.; Siperstein, F.R.; Pirngruber, G.; Nieto-Draghi, C.; Chaplais, G.; Simon-Masseron, A.; Bazer-Bachi, D.; Peralta, D.; Bats, N. Adsorption of $CO_2$, $CH_4$, and $N_2$ on zeolitic imidazolate frameworks: Experiments and simulations. *Chem. Eur. J.* **2010**, *16*, 1560–1571. [CrossRef]

114. Pantatosaki, E.; Pazzona, F.G.; Megariotis, G.; Papadopoulos, G.K. Atomistic simulation studies on the dynamics and thermodynamics of nonpolar molecules within the zeolite imidazolate framework-8. *J. Phys. Chem. B* **2010**, *114*, 2493–2503. [CrossRef] [PubMed]
115. Yusuf, K.; Badjah-Hadj-Ahmed, A.Y.; Aqel, A.; Othman, Z.A.A.L. Fabrication of zeolitic imidazolate framework-8-methacrylate monolith composite capillary columns for fast gas chromatographic separation of small molecules. *J. Chromatogr. A* **2015**, *1406*, 299–306. [CrossRef]
116. Grob, R.L.; Barry, E.F. *Modern Practice of Gas Chromatography*; Wiley & Sons: Hoboken, NJ, USA, 2004. [CrossRef]
117. Katz, S.; Gray, D.G. The adsorption of hydrocarbons on cellophane. I. Zero coverage limit. *J. Colloid Interface Sci.* **1981**, *82*, 318–325. [CrossRef]
118. Kazayawoko, M.; Balatinecz, J.J.; Romansky, M. Thermodynamics of adsorption of n-alkanes on maleated wood fibers by inverse gas chromatography. *J. Colloid Interface Sci.* **1997**, *190*, 408–415. [CrossRef] [PubMed]
119. Miller, K.J. Additivity methods in molecular polarizability. *J. Am. Chem. Soc.* **1990**, *112*, 8533–8542. [CrossRef]
120. Babarao, R.; Dai, S.; Jiang, D.E. Effect of pore topology and accessibility on gas adsorption capacity in zeolitic-imidazolate frameworks: Bringing molecular simulation close to experiment. *J. Phys. Chem. C* **2011**, *115*, 8126–8135. [CrossRef]
121. van der Perre, S.; van Assche, T.; Bozbiyik, B.; Lannoeye, J.; de Vos, D.E.; Baron, G.V.; Denayer, J.F.M. Adsorptive characterization of the ZIF-68 metal-organic framework: A complex structure with amphiphilic properties. *Langmuir* **2014**, *30*, 8416–8424. [CrossRef] [PubMed]
122. Devriese, L.I.; Martens, J.A.; Thybaut, J.W.; Marin, G.B.; Baron, G.V.; Denayer, J.F.M. A new methodology to probe shape selectivity in porous adsorbents. *Microporous Mesoporous Mater.* **2008**, *116*, 607–613. [CrossRef]
123. James, A.T. Vapour phase chromatography, edited by D.H. Desty. Butterworths scientific publications, London, 1957, 436 pages, price? 3.10s. *J. Chromatogr. A* **1958**, *1*, 203. [CrossRef]
124. Cavka, J.H.; Jakobsen, S.; Olsbye, U.; Guillou, N.; Lamberti, C.; Bordiga, S.; Lillerud, K.P. A new zirconium inorganic building brick forming metal organic frameworks with exceptional stability. *J. Am. Chem. Soc.* **2008**, *130*, 13850–13851. [CrossRef]
125. Bárcia, P.S.; Guimarães, D.; Mendes, P.A.P.; Silva, J.A.C.; Guillerm, V.; Chevreau, H.; Serre, C.; Rodrigues, A.E. Reverse shape selectivity in the adsorption of hexane and xylene isomers in MOF UiO-66. *Microporous Mesoporous Mater.* **2011**, *139*, 67–73. [CrossRef]
126. Senkovska, I.; Hoffmann, F.; Fröba, M.; Getzschmann, J.; Böhlmann, W.; Kaskel, S. New highly porous aluminium based metal-organic frameworks: Al(OH)(ndc) (ndc = 2,6-naphthalene dicarboxylate) and Al(OH)(bpdc) (bpdc = 4,4′-biphenyl dicarboxylate). *Microporous Mesoporous Mater.* **2009**, *122*, 93–98. [CrossRef]
127. Denayer, J.F.; Baron, G.V.; Martens, J.A.; Jacobs, P.A. Chromatographic study of adsorption of n-alkanes on zeolites at high temperatures. *J. Phys. Chem. B* **1998**, *102*, 3077–3081. [CrossRef]
128. Ruthven, D.M.; Kaul, B.K. Compensation theory of adsorption: Correlation and prediction of henry constants for linear paraffins on zeolite adsorbents. *Adsorption* **1998**, *4*, 269–273. [CrossRef]
129. Finsy, V.; Kirschhock, C.E.A.; Vedts, G.; Maes, M.; Alaerts, L.; de Vos, D.E.; Baron, G.V.; Denayer, J.F.M. Framework breathing in the vapour-phase adsorption and separation of xylene isomers with the metal-organic framework MIL-53. *Chem. Eur. J.* **2009**, *15*, 7724–7731. [CrossRef] [PubMed]
130. Finsy, V.; Verelst, H.; Alaerts, L.; de Vos, D.; Jacobs, P.A.; Baron, G.V.; Denayer, J.F.M. Pore-filling-dependent selectivity effects in the vapor-phase separation of xylene isomers on the metal-organic framework MIL-47. *J. Am. Chem. Soc.* **2008**, *130*, 7110–7118. [CrossRef]
131. Chen, K.J.; Madden, D.G.; Pham, T.; Forrest, K.A.; Kumar, A.; Yang, Q.Y.; Xue, W.; Space, B.; Perry, J.J.; Zhang, J.P.; et al. Tuning Pore Size in Square-Lattice Coordination Networks for Size-Selective Sieving of $CO_2$. *Angew. Chem. Int. Ed.* **2016**, *55*, 10268–10272. [CrossRef] [PubMed]
132. Xue, D.X.; Belmabkhout, Y.; Shekhah, O.; Jiang, H.; Adil, K.; Cairns, A.J.; Eddaoudi, M. Tunable rare Earth fcu-MOF platform: Access to adsorption kinetics driven gas/vapor separations via pore size contraction. *J. Am. Chem. Soc.* **2015**, *137*, 5034–5040. [CrossRef] [PubMed]
133. Xue, D.X.; Cairns, A.J.; Belmabkhout, Y.; Wojtas, L.; Liu, Y.; Alkordi, M.H.; Eddaoudi, M. Tunable rare-earth fcu-MOFs: A platform for systematic enhancement of $CO_2$ adsorption energetics and uptake. *J. Am. Chem. Soc.* **2013**, *135*, 7660–7667. [CrossRef] [PubMed]
134. Assen, A.H.; Belmabkhout, Y.; Adil, K.; Bhatt, P.M.; Xue, D.X.; Jiang, H.; Eddaoudi, M. Ultra-tuning of the rare-earth fcu-MOF aperture size for selective molecular exclusion of branched paraffins. *Angew. Chem. Int. Ed.* **2015**, *54*, 14353–14358. [CrossRef] [PubMed]
135. Shi, B. Problem in the molecular area of polar probe molecules used in inverse gas chromatography. *J. Chromatogr. A* **2019**, *1601*, 385–387. [CrossRef] [PubMed]
136. Brendlé, E.; Papirer, E. A new topological index for molecular probes used in inverse gas chromatography 2. Application for the evaluation of the solid surface specific interaction potential. *J. Colloid Interface Sci.* **1997**, *194*, 217–224. [CrossRef] [PubMed]
137. Legras, A.; Kondor, A.; Heitzmann, M.T.; Truss, R.W. Inverse gas chromatography for natural fibre characterisation: Identification of the critical parameters to determine the Brunauer–Emmett–Teller specific surface area. *J. Chromatogr. A* **2015**, *1425*, 273–279. [CrossRef] [PubMed]